The Thesis Committee for Cheng Zhao
Certifies that this is the approved version of the following Thesis:

A Bidirectional MEMS Thermal Actuator as the Building Block for a Programmable Metamaterial

APPROVED BY
SUPERVISING COMMITTEE:

Michael A. Cullinan, Supervisor

Jonathan B. Hopkins

A Bidirectional MEMS Thermal Actuator as the Building Block for a Programmable Metamaterial

by

Cheng Zhao

Thesis

Presented to the Faculty of the Graduate School of

The University of Texas at Austin

in Partial Fulfillment

of the Requirements

for the Degree of

Master of Science in Engineering

The University of Texas at Austin

August 2018

Dedication

To my friends and family, for their constant support.

Acknowledgements

I would like to thank my advisor, Dr. Michael Cullinan, for providing the opportunity to work on this project and having me as a member of the Nanoscale Design and Manufacturing Laboratory. His vast knowledge and astute guidance have been essential for the progression of my research and my perseverance through times of difficulty and self-doubt can be attributed to his kind and personable nature as well as his words of reassurance. I would also like to thank our collaborators at UCLA, Dr. Jonathan Hopkins and Yuanping Song, for their instrumental contributions and consistent support. This work was supported in part by the Air Force Office of Science Research and Byung "Les" Lee is gratefully acknowledged.

I would like to thank Chenyang Luo, Ian Ladner and Sridharan Thirumalai for their assistance and valuable contributions to various aspects of the project. Lastly, I would like to thank every member of the laboratory, all of whom I have come to form treasured friendships with, as well as those in the Mechanical Engineering department whom I have had the pleasure of interacting with for a very enjoyable time these past two years.

Abstract

A Bidirectional MEMS Thermal Actuator as the Building Block for a Programmable Metamaterial

Cheng Zhao, M.S.E.

The University of Texas at Austin, 2018

Supervisor: Michael A. Cullinan

This thesis presents a novel bidirectional MEMS thermal actuator that is intended to be implemented as the building block for a microarchitectured material. The successful proof of concept demonstrates the potential for a new level of miniaturization for the technology that would improve existing capabilities and enable new ones. The design is built upon the bent-beam type thermal actuators with an emphasis on large travel and force output. Sensing capabilities are accomplished through piezoresistive strain gauges that provide sufficient sensitivity and resolution. An analytical model was created to calculate the performance parameters of actuator designs and was used in conjunction with optimization software to arrive at four selected designs with minimal theoretical trade-offs. Successful fabrication of the devices was achieved with standard microfabrication techniques. Preliminary testing results have demonstrated the successful operation of bidirectional actuation and confirms the validity of the concept.

Table of Contents

List of Tables

List of Figures

Chapter 1: Introduction

The purpose of this project is to develop a novel MEMS (microelectromechanical system) actuator that can be utilized as the building block for a microarchitectured material with shape morphing capabilities and programmable properties. The successful proof of concept would provide the gateway into a new level of miniaturization for the constituent unit cells of metamaterials and enable a wider range of applications for the emerging technology with its increased resolution and smaller device footprint.

1.1 Background and Motivation

A microarchitectured material consists of a repeating lattice of unit cells that interact to form desired bulk properties [1]. Through creative designs of such unit cells, the microachitectured material can be capable of exhibiting extraordinary properties such as high strength-to-weight ratios and extreme or even negative thermal expansion coefficients [2]. Going beyond traditional passive composite materials that rely solely on the topology and properties of their constituent flexible elements, a new class of externally powered metameterials are emerging that couple sensing and actuation to achieve reconfigurable shape morphing and programmable material properties [1].

A material that is reconfigurable based on functionality can have many potential applications. For example, if implemented as the surface material for aircrafts or high-speed vehicles, it can actively deform its shape or surface texture to increase maneuverability, decrease drag and improve fuel efficiency. The ability to have real-time control of material properties such as elastic modulus would also be desirable for applications such as endoscopic biomedical tools that become compliant in certain areas but stiffen in others when rigidity is required. Other applications can include braces and prosthetics to provide active damping, soft and sensorial robotics, vibration isolators and acoustic metamaterials [3].

1.1.1 Existing Microarchitectured Materials

Although most examples of compliant lattice materials are passive, there are a few existing examples of modular robotic cells that achieve shape morphing through detachment and reattachment at different locations within the lattice using mechanical latches [4], magnetic forces [5] and fluid flow [6]. Although such methods allow for drastic shape transformations, the friction produced through detachment, movement and reattachment precludes the material from performing high precision applications [1]. Thus, microarchitectured materials that produce relative motion and gradual transformations over larger length scales through the small deformation of unit cells that always remain attached to their neighboring cells are suitable for precision applications. Furthermore, by programming each unit cell to respond to external loads in a specific way, tunable material properties such as infinite or negative stiffness and negative Poisson ratio can be achieved [1]. The goal of the project is to develop a microarchitectured material of this type.

Examples of existing prototypes of this material type include one utilizing electrically switched electromagnetic engagement [7] and another utilizing piezo actuators [3]. Both are shown in Figure 1.1 and Figure 1.2.

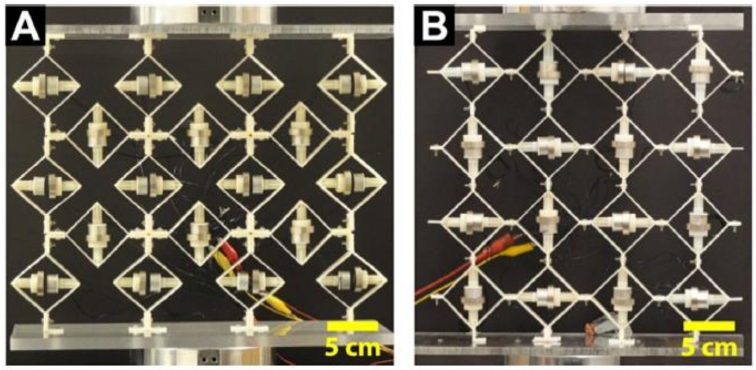

Figure 1.1: Programmable metamaterial using electromagnetic engagement.

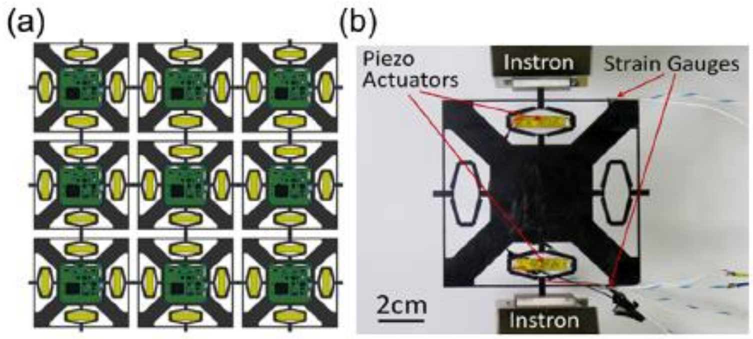

Figure 1.2: Programmable metamaterial using piezo actuators.

As shown, both examples are prototypes in the macroscale with the device footprint of each unit cell being around 5 cm × 5 cm. Simply due to their size, many potential applications such as endoscopic tools would not be possible and the smallest texture resolution or the smoothness of shape transition over a given length or surface area is necessarily limited. Materials constructed with large unit cells also do not appear material-like due to how distinct and obvious each constituent element is. Furthermore, due to the sometimes binary nature of actuation such as in the first example with engagement vs. disengagement, it may be impossible to achieve an analog range of material property values. Finally, most prototypes only exist as planar materials and examples of designs that support 3D assemblies are rare.

Thus, to create programmable metamaterials with microscale unit cells, the actuation and sensing mechanisms need to be miniaturized as much as possible. The capability of MEMS actuators and sensors as well as their ability to be integrated on a single chip makes them a good choice for the application and the maturity of microfabrication techniques ensure the opportunity for a wide range of designs to be realized.

1.1.2 MEMS Actuators

MEMS actuators with force and axial displacement outputs can be categorized into four main families: electrostatic, thermal, piezoelectric and magnetic. Table shows the various design considerations for the selection of actuator type.

Table 1.1: Considerations for actuator selection.

Actuator	Force	Travel	Fabrication	Switching	Energy Consumption	Implementation
Electrostatic	Low	Large	Simple but with potential for difficulties	Fast	Low	Easy
Thermal	High	Large Based on design	Simple	Slow	High	Easy
Piezoelectric	High	Low	Complex	Fast	Low	Easy
Magnetic	High	Large	Complex	Medium	High	Hard

The most desirable traits for the actuators from the metamaterial perspective would be high travel to maximize the range of shape morphing capabilities and high force output to be able to respond and counteract larger external loads. A larger force output also correlates to higher inherent stiffness which provides more structural rigidity and robustness as an assembled material. Furthermore, manufacturability is also critical and fabrication of the actuators should be possible with standard microfabrication techniques and materials available at the designated facility.

Electrostatic actuators are considered the most common choice for microactuators [8], with electrostatic comb drives being the most prominent configuration for in-plane motion. The working principle is actuation produced by the electric field of a capacitor, where a voltage is applied between two interdigitated finger structures, one fixed and the other connected to a compliant suspension, and deflection of the movable comb structure is induced by the electrostatic forces generated between the plates [9]. While capable of producing large displacements up to 20 μm [10], their force output is relatively low (rarely exceeding 10 μN) and require very large areas to have increased arrays for extra force output [11]. Furthermore, although consuming no current and operating at low power, they require high voltages (>30 V) which can be incompatible with certain standard electronics [12]. Finally, although the fabrication for comb drives is generally simple, a large number of fingers with relatively small feature sizes and tight tolerances in addition to thin flexures to provide compliance could potentially result in difficulties especially if deep silicon etching is involved. A release step is also required for the suspended structure and potential stiction issues may occur.

Thermal actuators rely on the thermal expansion of materials to produce displacement. The type of thermal actuator under consideration is not the bimorph which is generally made for out-of-plane actuation but the bent-beam or chevron beam thermal actuators. Figure 1.3 shows the structure and operation of the bent-beam thermal actuator where current is passed through a V-shaped beam anchored at its two end and thermal expansion caused by joule heating pushes the apex outward [12]. Standard configurations can achieve around 10 μm of displacement and can be improved by multiple factors with optimized and cascading designs [11]. While there is potentially a slight trade-off in terms of travel, the bent beam thermal actuators easily offer 10-100× improvement in terms of driving force compared to the electrostatic actuator [11]. Fabrication is also simple as only limited number of beams need to be etched and there is no suspended structure if utilizing the whole wafer as beam material. The disadvantages of the thermal actuator lie in its high power consumption and low switching speeds [12]. Since the goal at this stage is a proof of concept and not necessarily commercialization, a higher power consumption is not considered a significant reason to sway away from the choice and optimization on power efficiency can be explored once the design has been validated. Thermal actuators are also generally limited to frequency responses less than 1000 Hz because of the time constants associated with heat transfer [10]. This trade-off is considered to be relatively inconsequential as based on the applications, extremely fast switching speeds are not required and there is much higher demand on the steady state response and static displacement.

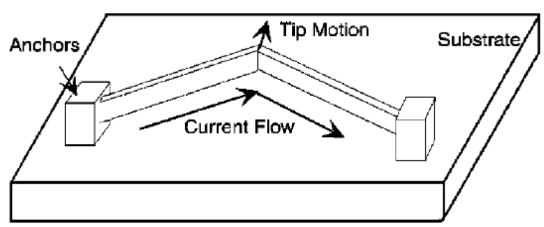

Figure 1.3: Structure and operation of a single bent-beam thermal actuator.

Piezoelectric actuators have the disadvantage of having lower travel and force output tied to its volume, which is especially troublesome as the deposition of piezoelectric materials tend to be nontrivial [13]. Magnetic MEMS actuators also require materials that are not necessarily easily deposited with MEMS fabrication techniques and processing is not CMOS compatible [14]. Designs also tend to be very complex and difficult to implement, especially to achieve in-plane actuation. Thus, neither piezoelectric and magnetic MEMS actuators were considered attractive choices for type selection.

1.2 Proposed Design Summary

Based on the criteria mentioned, the bent-beam thermal actuator was selected as the optimal choice for the constituent element for the microarchitectured material. A novel design based upon the actuator type was contrived that increases the travel range and versatility of the shape morphing capability through the cascading of two chevron beam structures and the ability to achieve bi-directional actuation. Actuation beams are fabricated using the entire thickness of the substrate which maximizes the stiffness of the structure while also eliminating the necessity for device release. Sensing is achieved through piezoresistive strain gauges fabricated on flexure beams connected to the tip of the actuator. Detailed description of the design can be found in Chapter 2.

1.3 Scope

This thesis focuses on the realization of the MEMS thermal actuator device that is to be implemented as the building block for the microarchitectured material. Chapter 2 describes the overall design and operation of the device as well as design of the piezoresistive strain gauge force sensors. Chapter 3 details the development of an analytical model to predict the actuator performance, the optimization process that enabled design selection and comparison of selected results with commercial FEA. Chapter 4 discusses the fabrication process of the devices with an emphasis on deep silicon etching. Chapter 5 presents preliminary testing results of successfully fabricated devices and Chapter 6 summarizes the outcomes of this project and outlines future work.

Chapter 2: Device Design

2.1 Overview

Based on the desired final product, an optimal actuator design should have bidirectional in-plane movement capabilities that, when implemented as faces, culminates in a cube that can expand or shrink in all three axes. While technically all thermal actuators are bidirectional, in that if a partially-powered state is considered the zero-displacement point then higher and lower power would result in relative expansion and compression, one in which the unpowered state can be considered the zero-displacement point would be desirable. If accomplished, the actuators would not require continuous power supply in order to have relative negative displacement and the total range of travel would not be limited by the full stroke. Thus, one of the major design goals is to develop an actuator that is capable of bidirectional displacement with respect to the unpowered state.

In addition to the bidirectional capability, the actuator should meet certain performance criteria that make it worth pursuing. For example, the range of travel for the actuator should at least exceed that of the bulk material when undergoing thermal expansion to justify a specific design. Other specifications and considerations include inherent stiffness, force output, overall package size, feature sizes and film thicknesses based on fabrication capabilities, all of which will be discussed further in chapters 3 and 4.

2.2 Device Description

2.2.1 Proposed Design

Figure 2.1 in the following page shows the baseline design for the device which exhibits all the components but does not have optimized parameters. Figure 2.2 shows the conceptual unit cell cube formed using the device as well as a 3×3×3 lattice material.

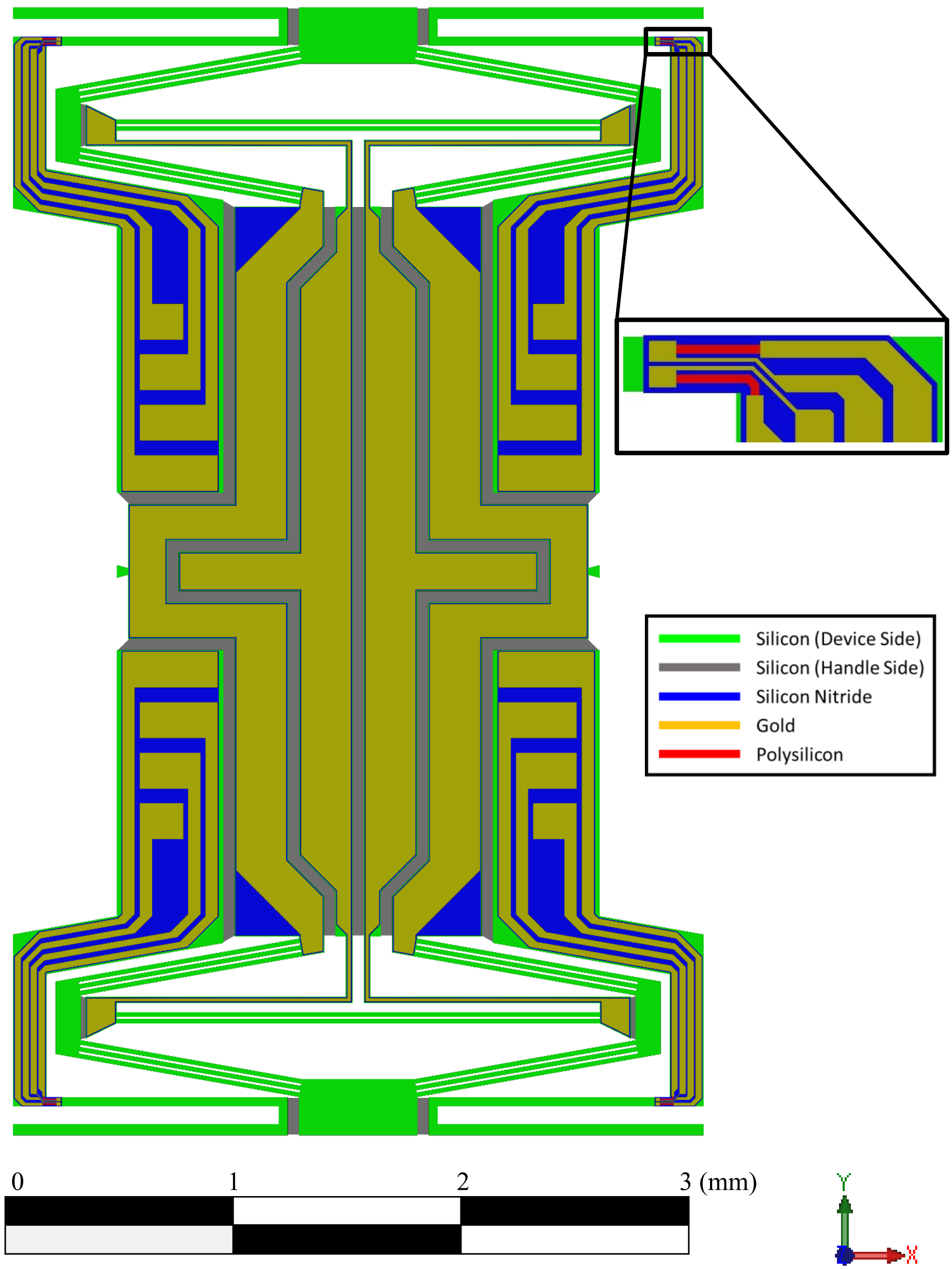

Figure 2.1: Baseline Device Design. Magnified portion shows strain gauges.

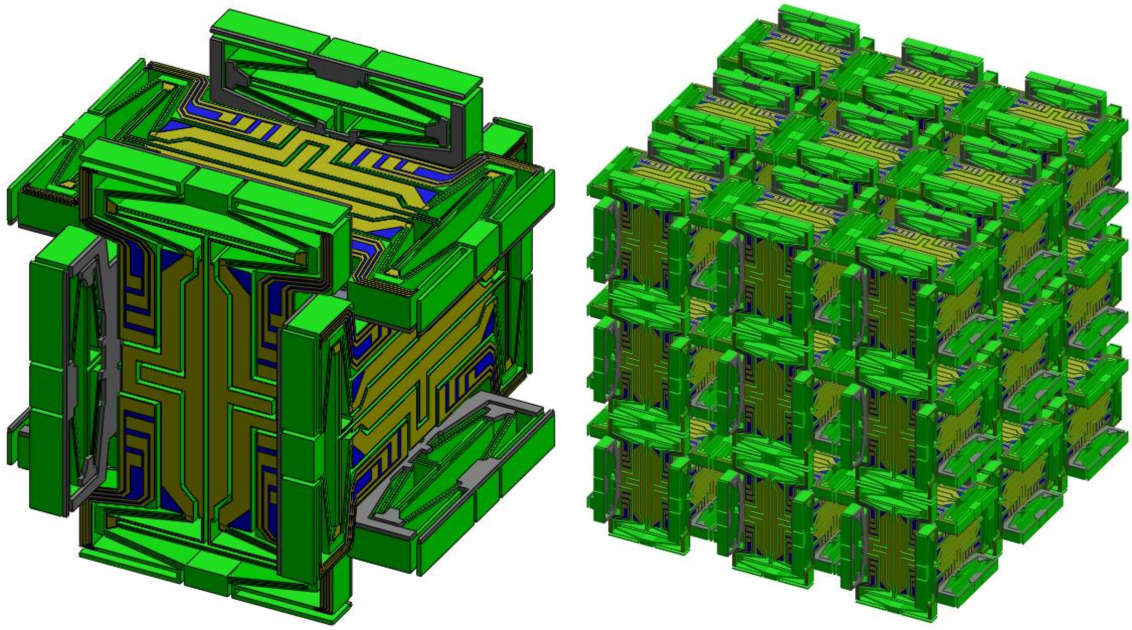

Figure 2.2: (Left) Conceptual unit cell cube. (Right) 3×3×3 lattice material.

2.2.1 Device Elements

The device can be broken down into three major constituent parts: the thermal actuators at the two ends of the device, the body of the device where gold bond pads are located, and polysilicon strain gauges located on flexure beams at both ends of the device.

Each of the thermal actuators contain two actuating components: the outer actuator and inner actuator, both contained within the outermost enclosure. The outer actuator consists of a pair of mirrored multi-chevron beam structures connected at the anchor, forming a diamond shape, and the inner actuator is a set of horizontal beams connecting the anchors through the handle silicon layer. The center portion of the device contains the metallic electrodes that would allow external electrical connections to pass current to the actuator or to acquire readings from the piezoresistive strain gauges. The handle side of the body is used to attach to a PCB or faces of the cube without potentially damaging features on the device side. Finally, a pair of polysilicon piezoresistive strain gauges can be found on each of the enclosure flexure beams connecting to the tip, the details of which will be discussed in section 2.3.

2.2.2 Materials

The device makes use of a SOI (Silicon on Insulator) wafer as the base substrate which has a buried silicon oxide layer between two silicon layers. Specifications for the selected SOI wafer can be found in Appendix A. The thicker silicon layer is used as the device layer and as the construction material for the thermal actuator. The thinner silicon layer is used as the handle layer that keeps different sections of the device layer mechanically connected and to provide an interface for attachment to the PCB or cube face. The design takes advantage of the buried silicon oxide layer to electrically insulate the two silicon layers and by selectively etching the two layers and creating connections that go from the device layer to the handle layer and then back, it is possible to apply current to distinct portions of actuator while keeping them mechanically attached.

Silicon nitride, followed by gold, is deposited, patterned and etched or lifted-off over portions of the actuator. The silicon nitride acts as electrical insulation that directs current to flow through the targeted joule heating components while also providing thermal resistance for the gold layer. Silicon nitride is also chosen as the dielectric material instead of silicon dioxide due to the need for HF dips in the process. Gold traces are patterned and used to direct current to flow through the actuation beams from external electrical connections. Gold was selected as it is the standard electrode contact material and allows for relative ease in wire bonding. As shown in Figure 2.3, where the gold layer is hidden, it can be seen that there is an open pocket in the silicon nitride layer such that the gold layer is in contact with the device layer at the two ends of the inner actuator beams. Similar setup is located at the ends of the outer actuator beams. This ensures that although the bonding site is at the center of the device, the current only flows through the actuator beams and is insulated from the rest of the device.

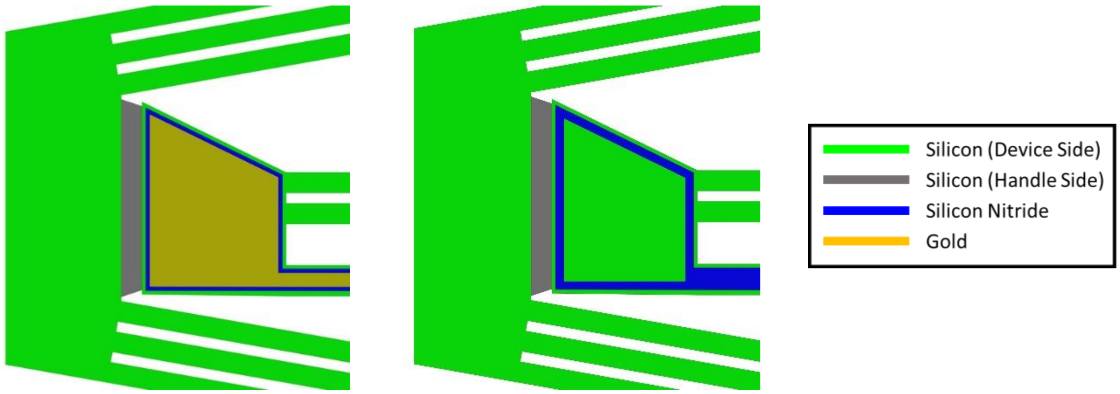

Figure 2.3: (Left) Anchor portion with gold showing. (Right) Anchor portion without gold showing.

2.2.3 Mode of Operation

When a voltage is applied across the two outer electrodes, current flows through the outer actuator while being electrically insulated from the inner actuator and the chevron beams undergo joule heating and thermal expansion. The outward horizontal motion in the x-direction at the anchors is restricted by the inner actuator beams, resulting in an upwards displacement at the tip of the device. Conversely, when a voltage is applied across the two inner electrodes, current flows through the center beams. The thermally expanded horizontal beams push the anchors outwards which results in a downwards displacement at the tip of the device. To minimize the number of external connections needed, the two thermal actuators at ends of the device share the same electrodes and in turn voltage drop as well, leading to symmetrical displacement at the two ends.

2.3 Polysilicon Piezoresistive Strain Gauges

2.3.1 Sensor Type Selection

A method of detection for the tip displacement is necessary to be able to evaluate the performance of the actuator as well as for future implementation of feedback control. Typical sensing methods for nano-Newton force resolution scale include piezoresistive, capacitive or optical/laser detection [15]. The optical method would not be practical for this application due to the necessity of an optical system for each of the actuators in the assembly. The capacitive method tend to require large sensor areas to achieve high dynamic range [16] and would most likely require an isolated structure that is stationary with respect to the moving tip. Attempting to incorporate such a structure to the device may lead to unnecessary complexity in its design and circuitry as well as more stringent fabrication requirements to ensure complete isolation between two electrodes. Thus, the piezoresistive method was chosen due to its high resolution and relative ease of implementation. Polysilicon was selected as the material due to it having higher sensitivity than other metal-based films, can be deposited easily on the silicon nitride insulating layer [17] and can reach the desired resistivity level through post-deposition doping.

2.3.2 Strain Gauge Configurations

The location selected for the strain gauges is on the flexure beams connected to the tip which act as part of the enclosure for the actuator. As shown in Figure 2.1, the flexure beam is analogous to that of a cantilever with the strain gauges located at the fixed end and the force generated by the actuator tip being applied at the free end. Due to the fact that the tip does not undergo any rotation and the angle of the end of the flexure beam attached to the tip is fixed, the free end would actually be more accurately considered as a guided constraint in this case. It should also be noted that the strain gauges would be used to measure the lateral force generated at the actuator tip in the y-direction, parallel to the wafer surface. There are two strain gauges on each flexure beam, each being equidistant from the center axis of the beam which results in one experiencing tension and the other in compression of equal magnitude regardless of the tip displacement. Thus, each actuator at the two ends of the device have four strain gauges with the two pairs theoretically having equivalent output values due to device symmetry and assuming that the actuator tip only moves in the vertical y-direction. This yields a total of eight for the whole device.

With the four strain gages for each actuator, there are options as to which bridge configuration to implement. The naming convention in the following figure will be used.

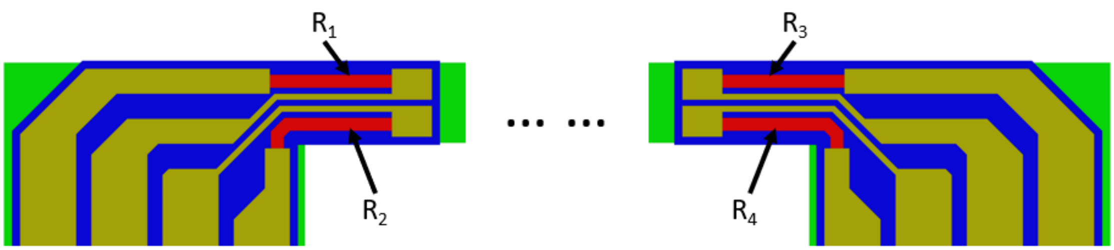

Figure 2.4: Naming convention to identify each strain gauge.

The bridge configurations in the Figure 2.5 can all be implemented, where R_f are fixed value resistors that are not actively measuring strains and can either be fabricated onto the device to complete the circuit or be part of an external bridge completion system.

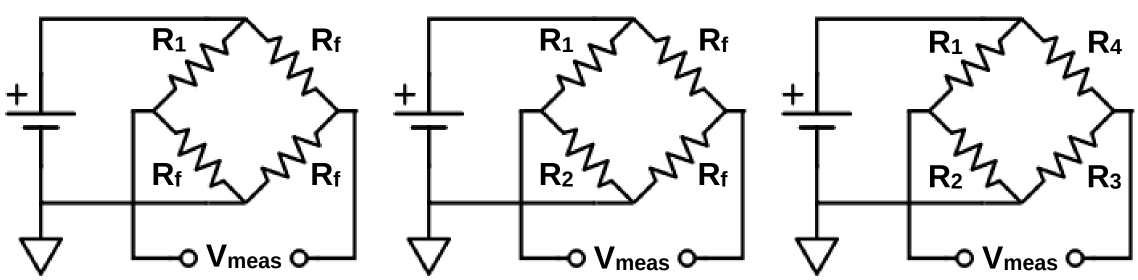

Figure 2.5: Bridge configurations. (Left) Quarter Bridge. (Center) Half Bridge. (Right) Full Bridge.

For the quarter bridge configuration, there is only one active strain gauge where R_1 could be replaced by any of the other strain gauges. In the half bridge configuration, R_1 and R_2 could be replaced with R_3 and R_4 for the other pair of strain gauges. The full bridge utilizes all four of the strain gauges designated for each actuator. The quarter bridge configuration requires distinct traces at both ends of the resistor which has been the design shown thus far with two bond pads for each strain gauge. For the half bridge and the full bridge, however, the strain gauges on either flexure beam share a node and thus two of the gold traces can be combined to one, resulting in only three bond pads for each pair of strain gauges on either side of the device. This design is shown in Figure 2.6 below.

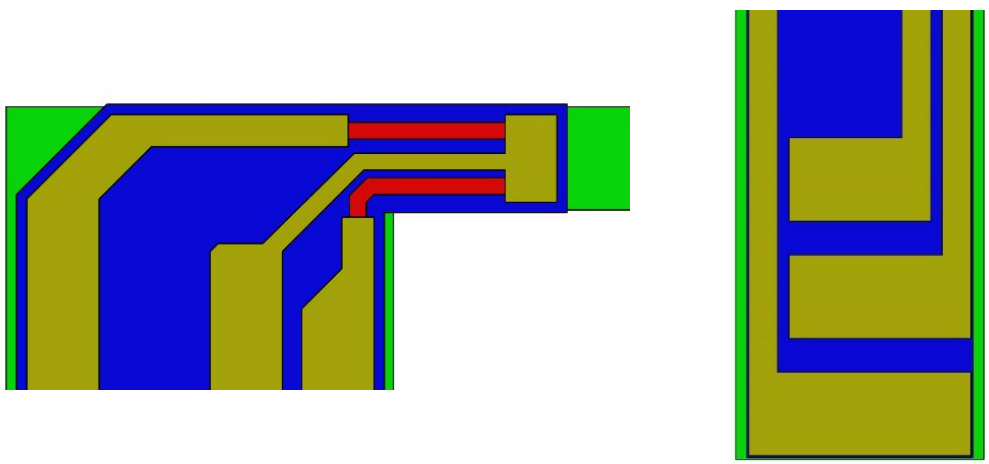

Figure 2.6: Half bridge and full bridge design. (Left) Strain gauge site. (Right) Bond pad site.

All presented configurations only measure the bending strain of the flexure beam with the quarter bridge having the lowest sensitivity and the full bridge having the highest. Poisson effects are not measured and ideally the quarter bridge also has a dummy resistor at the strain gauge site to compensate for temperature effects but due to limited design space it was neglected for the time being. While the full bridge configuration has the highest sensitivity and requires the least amount of auxiliary bridge elements, it requires proper functionality of all four strain gauges as well as symmetrical tip force for both flexure beams. Thus, in the case that it may be desirable to observe individual strain gauges, both versions of the design (three bond pads and four bond pads for each strain gauge pair) are kept for fabrication.

2.3.3 Piezoresistive Strain Gauge Design

For a lateral force applied at the roller end of the flexure beam, the relative change of the piezoresistance is given by Eq. 1 [15], where R is the resistance of the piezoresistor and can be calculated with the resistivity value based on doping and its geometric parameters, π_l is the piezoresistive coefficient with a value of 55.8×10^{-11} for longitudinal, n type, and random orientation [18], F is the force applied, z is the distance from the piezoresistor to the neutral axis of the beam, L, W, H are geometric parameters for the flexure beam and l is the length of the piezoresistor. It should be noted that the $\frac{L}{2}$ term was used instead of the standard L is due to the flexure beam not being a true cantilever and having a guided end condition.

$$\frac{\Delta R}{R} = \frac{12\pi_l F z}{W^3 H}\left(\frac{L}{2} - \frac{l}{2}\right) \tag{1}$$

For a half bridge configuration, the sensitivity can be calculated using Eq. 2, where V_{cc} is the supply voltage (assumed to be 10 V).

$$V_{out} \approx \frac{V_{cc}\Delta R}{2R} \tag{2}$$

Using a theoretical force of 1 N, the voltage outputs for the four actuator designs to be presented in the follow chapter range from the lowest sensitivity value of around 0.5 V/N to the highest sensitivity value of around 10 V/N. Results are calculated using a resistivity value of 3E-5 Ω/m and all piezoresistors adjusted in terms of geometry to have a resistance of 1 kΩ. Variation in values is the result of having different geometric parameters for the flexure beams and piezoresistors.

The noise voltage in an assumed frequency band between 1 Hz and 1 kHz is given by Eq. 3 [15], where the noise components including Johnson, flicker and that of the amplifier are the terms within the square root, respectively.

$$V_n = \sqrt{4k_B TR(f_{\max} - f_{\min}) + \frac{\alpha V^2}{c_i lwt}\log(\frac{f_{\max}}{f_{\min}}) + S_{Vai}(f_{\max} - f_{\min})} \qquad (3)$$

k_B is the Boltzmann constant, T is the ambient temperature, V is the bias voltage across the resistor, f is the frequency, α is the Hooge constant, c_i is the charge carrier concentration, l, w, t are the piezoresistor length, width, and thickness, respectively and S_{Vai} is PSD of amplifier input voltage noise [16]. Using approximated values where necessary, the largest value out of the selected designs for the minimum detectable force can be estimated to be 5 μN. Based on predicted values presented in the next chapter, the force outputs are expected to be within the range of 0.1 N to 1 N and thus the sensor resolution is more than sufficient.

Chapter 3: System Modelling and Optimization[1]

3.1 Introduction

The operation of the device starts in the electrothermal domain which then extends into the mechanical domain. A complete analytical model that covers the mentioned domains was created in MATLAB in order to gain an understanding of how the geometric parameters influence the performance of the actuator as well as be able to predict the expected actuator outputs based on given designs and inputs. The developed model is finally used in conjunction with optimization software to determine designs with minimal trade-offs in performance. It is worth noting that analytical modelling tends to be highly idealized, especially in this case, and is likely to produce solutions that do not necessarily conform to experimental results to a high degree. While having highly accurate prediction results are desirable, the main goal of the analytical model is to provide a guideline and method for device design selection.

3.2 Previous Methods

Traditional modelling methods for the chevron-beam thermal actuators consisted of electrothermal and solid mechanics FEA, often times with complementary analytical modelling using derived beam equations [11], [12], [19]. This has consistently been the selected approach for such structures which examines the barebone of the actuator, consisting of the anchors, the beams and the shuttle. Zhu et al. utilized multiphysics FEA which used the voltage difference across the anchors as input and generated the temperature

---

[1] Zhao, C., Ladner, I.S., Song, Y., Hopkins, J.B., Cullinan, M.A., "Design and Modeling of a Bidirectional Thermal Actuator," *Proc. of the 32nd Annual Meeting of the American Society for Precision Engineering (ASPE)*, Charlotte, NC, October 2017.
Author contribution include the development of the analytical model, result comparison and writing of the publication.

profile throughout the actuator. The temperature increase is then used to simulate thermal expansion of the beams which led to the displacement of the shuttle. A sample FEA simulation result from their study is shown in Figure 3.1.

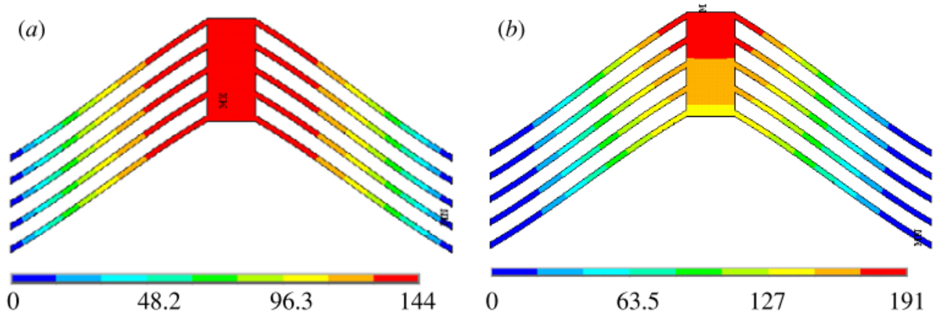

Figure 3.1: Sample FEA result from Zhu study [20]. (a) Temperature increase field (in ∘C) and (b) displacement field (in nm) in the thermal actuator.

In terms of analytical modelling, the following model is generally implemented where due to symmetry only beams on one side are observed, with the anchor acting as a fixed support condition and the shuttle end of the beam having only one degree of freedom in the axial direction.

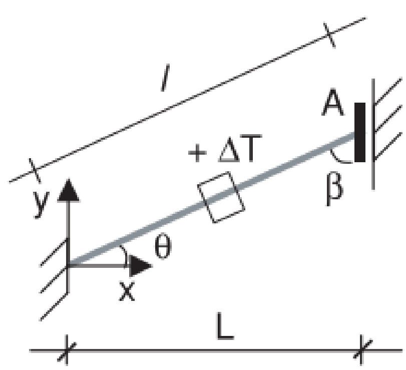

Figure 3.2: Mechanical representation of a single beam from Zhu study [20].

General beam bending equations, strain energy calculations and assembly of its stiffness matrix can all be used to solve for the displacement of the beam end at the shuttle and will not be discussed in detail here.

The aforementioned approach to modelling has several shortcomings, especially if it were to be implemented on the actuator design proposed in this project. The proposed actuator design is much more complex than the basic chevron-beam thermal actuator and has eleven optimizable geometric variables (discussed in detail in section 3.3.1) instead of only three which are the length, width and angle of the beam. While it is possible to model the actuators completely using FEA software, relatively complex multi-domain simulations are needed for each of the designs based on the high number of optimization variables which would require immense computational power and time. Traditionally, analytical modelling only applies to the mechanical domain after temperature profiles have already been obtained from FEA software. Ideally, even the necessity to rely on electrothermal results from FEA software should be eliminated and a full analytical model with fast calculation times would be fitting.

Furthermore, analytical models such as the one in Figure 3.2 would not be sufficient for the actuator design in this case since the anchors are no longer fixed supports and can undergo translation and rotation which would affect the bending of the slanted parallel actuator beams. The increased complexity from studying single beams to the beam structure in this design calls for a different approach in solving for the mechanical behavior of the actuator.

3.3 Analytical FEM Model

The entirety of the analytical model is created in MATLAB and the overall simulation can be broken down into three models: the electrical model which calculates the power of heat generated by the passage of current through the actuator, the thermal model that calculates the temperature profile of the actuator from joule heating and the mechanical model which calculates the displacement of the actuator from its thermal expansion, its inherent stiffness as well as the theoretical force output. All models are formulated in some form of FEM where the entire system is subdivided into smaller parts consisting of nodes and links.

3.3.1 Geometry Generation

The bidirectional thermal actuator portion of the device can be seen in Figure 3.3. The labels (with symmetry applied) will act as the naming convention for the components herein. The outer actuator encompasses the enclosing outer silicon portions, namely the tip, upper beams, outer portion of the anchor and the lower beams. The inner actuator consists of the center beams as well as the two connection beam segments that are used to pass current to the center beams.

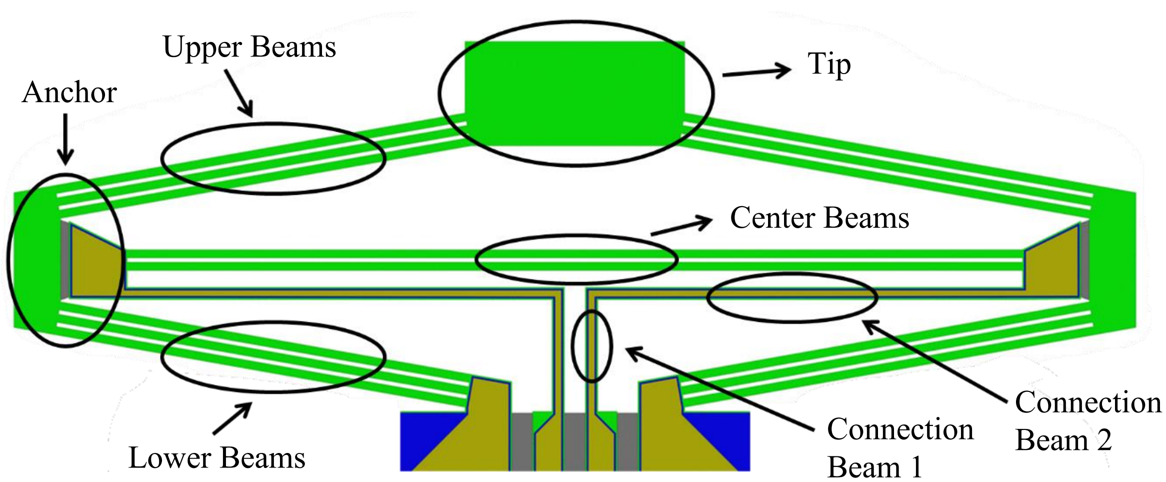

Figure 3.3: Thermal actuator portion of device.

In order to begin analyzing the system it is necessary to acquire the geometry and dimensions to the specific actuator design. The total device area is designed to not exceed beyond a 5.5 mm × 4 mm envelope, with most designs having exactly 5 mm in length and in the range of 3 ± 0.5 mm in width. The thermal actuator itself is contained with an envelope of 1.5 mm × 3.25 mm to ensure sufficient space for bond pad sites at the center of the device as well as to avoid potential collision of the anchors with the outer enclosure structure under operation. Other dimensional guidelines include a fixed gap distance between the beams, a fixed distance between the ends of the inner actuator to the outer actuator at the anchor and a few others to add some constraint to the possible designs as well as to standardize them to a degree.

Yuanping Song from UCLA was responsible for the development of the MATLAB script that generates actuator designs by varying a set of 11 governing geometrical parameters, namely the length, width and number of top, bottom and center beams, and the angles of the top and bottom beams. The constraints on the parameters are then derived according to the positions of the solid bodies such that there are no overlapping or interfering structures. Other geometric dimensions of the device that are not fixed are adjusted accordingly to accommodate for the 11 changing variables. The output geometries are formed by connecting vertices of known coordinates which are used as input to set up the analytical model structures. A table containing the range and resolution of the parameters can be found in Appendix B.

3.3.2 Electrical Model

The thermal actuator itself can be thought of as a resistor circuit whereby the resistive elements undergo joule heating and produce heat. Figure 3.4 shows the equivalent resistor circuits of the outer and inner actuators which can both be powered independently.

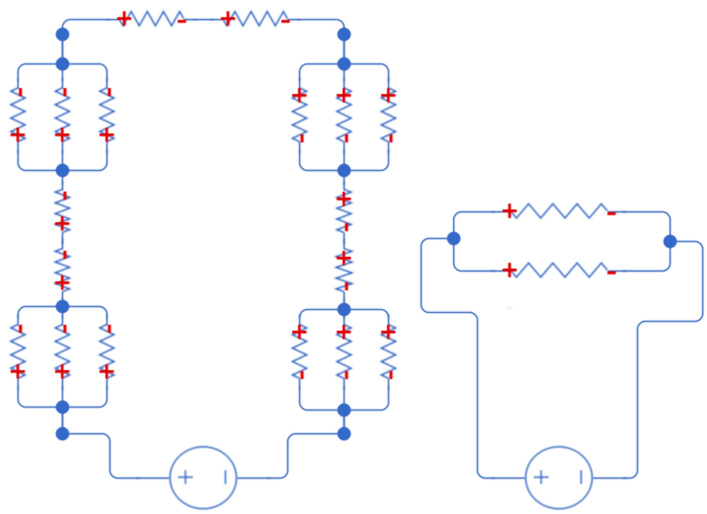

Figure 3.4: Equivalent resistor circuits for outer (left) and inner (right) actuators of baseline design.

As shown, the parallel actuator beams are also modelled as parallel resistors within the circuit, with the anchor portion of the outer actuator as well as the tip taken into consideration as extra resistors. The generated geometries make it possible to determine the resistance values of the beam elements through Eq. 4, where R is the resistance, ρ is the resistivity of the resistor material, L is the length of the segment and A is the cross-sectional area of the segment. The resistivity value used in this case is 0.0002 ohm-m which is the upper range limit given by the SOI wafer specifications sheet. Calculations were done with the resistivity as a fixed value due to the complex nature of its dependence on temperature for extrinsic semiconductors as well as inconsistencies in doping concentration. Incorporating temperature dependence for the resistivity also necessitates an iterative solution which would lead to a significantly higher computation time.

$$R = \rho \frac{L}{A} \tag{4}$$

To determine the heat power, P, generated by each resistor, the Joule heating equation for direct current, Eq. 5, is used, where the voltage across the resistors, V, can be found by solving the circuit through the electrical model written in MATLAB. The electrical model is an implementation of nodal analysis using Kirchoff's current law based on a pre-existing circuit solver script [21].

$$P = V^2 / R \tag{5}$$

3.3.3 Thermal Model

At the early stage of the device development, the thermal analysis focused primarily on the steady state response with less focus on the transient response. Since the actuator stroke as well as force output are considered the primary design objectives and both dependent only on the final thermal expansion of the beams, time and frequency response as well as switching speeds are to be subjects of future investigation.

The three modes of heat transfer were investigated to determine the relative effect each had on the final steady-state temperature of the device. Conduction is undoubtedly the most significant mode of heat transfer given that the actuator operates under joule heating and internal heat conduction. Microscale convective coefficients is experimentally shown to be higher than that of macroscale [22]. Preliminary FEA studies with air convection set to all surfaces with heat transfer coefficient of $h \approx 40$ W/m^{2}K had an effect on the temperature profiles of the actuators of about 2% - 5% compared to the no convection simulations. Furthermore, heat loss through radiation in MEMS devices of this scale is expected to be minimal even at high temperatures (1000 ^{o}C) [23], affecting less than 1% of the temperature profile with rough calculations. Thus, conduction is considered to be the most prominent heat transfer mechanism by far and a 1-D conduction bar element FEM model was selected for the estimation of actuator temperature profiles. This is also a convenient choice due to the similar system structure setup as the electrical and the upcoming mechanical model.

A 1-D conduction FEM model representation of the whole actuator consisting of nodes and bar elements is formed. The structure is very similar to that of the electrical circuit model, with the additional aspect of combining both outer and inner actuators instead of viewing each separately based on the mode of operation as they are not thermally insulated despite being electrically insulated. A visual representation for the baseline actuator is shown in Figure 3.5.

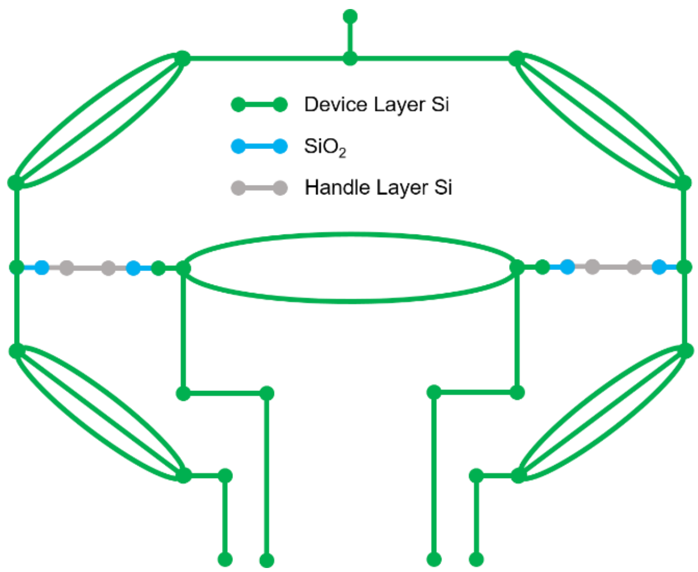

Figure 3.5: Visual representation of 1-D conduction model for baseline actuator. Not drawn to scale.

As shown, the connection between the outer and the inner actuators goes through the buried silicon oxide and the handle silicon layer, with the silicon oxide having a significantly lower thermal conductivity value, $k_{SiO_2} = 1.4\ \text{W/mK}$, than that of silicon, $k_{Si} = 148\ \text{W/mK}$. Again, although the thermal conductivity values are functions of temperature, the values at 300 K are used as constants for the same reasons as the resistivity value. The center portion of the device is also accounted for as extra bar elements because the boundary condition at the nodes where the voltage is applied is not necessarily that of room temperature.

To solve for temperatures at the nodes, the Fourier heat conduction equation, Eq. 6, is used where q is the rate of axial heat flow, k is the conductivity of the material, T is temperature and x is the distance along the element. This equation is then used to relate nodal temperatures to nodal heat flows in the matrix form, Eq. 7. [24], where the subscript 1 and 2 denote the two ends of a bar element.

$$q = -Ak\frac{dT}{dx} \tag{6}$$

$$\begin{bmatrix} Ak/L & -Ak/L \\ -Ak/L & Ak/L \end{bmatrix}\begin{Bmatrix} T_1 \\ T_2 \end{Bmatrix} = -\begin{Bmatrix} q_1 \\ q_2 \end{Bmatrix} \tag{7}$$

The square matrix is the element conductivity matrix, analogous to stiffness matrix of structural mechanics, which is generated for each element in the model using the known heat flow inputs, actuator geometry, as well as the set boundary conditions and assembled into the global conductivity matrix in the manner of Eq. 8, where K are the corresponding components in the element conductivity matrix.

$$\begin{bmatrix} K_1 & -K_1 & \cdots & 0 \\ -K_1 & K_1 + K_2 & & \\ \vdots & & \ddots & \vdots \\ 0 & & \cdots & K_N \end{bmatrix}\begin{Bmatrix} T_1 \\ T_2 \\ \vdots \\ T_{N+1} \end{Bmatrix} = -\begin{Bmatrix} q_1 \\ q_2 \\ \vdots \\ q_{N+1} \end{Bmatrix} \tag{8}$$

The boundary condition assumes that the center of the devices will remain at room temperature. Five nodes, spaced evenly, are added to the middle of the bar elements, splitting each into six segments. With this procedure, the input heat flow derived from the electrical model is divided and applied among the five nodes to replicate the joule heating effect. Doing so also allows for a more detailed temperature profile result where the temperature at certain points along each element can be probed. Finally, the global conductivity matrix is rearranged and partitioned as given in Eq. 9, where α and β refer to unknown and known temperatures. Solving Eq. 10 results in the temperatures at the nodes where they are not known.

$$\begin{bmatrix} [K_{\alpha\alpha}] & [K_{\alpha\beta}] \\ [K_{\beta\alpha}] & [K_{\beta\beta}] \end{bmatrix} \begin{Bmatrix} \{T_\alpha\} \\ \{T_\beta\} \end{Bmatrix} = - \begin{Bmatrix} \{q_\alpha\} \\ \{q_\beta\} \end{Bmatrix} \tag{9}$$

$$\{T_\alpha\} = [K_{\alpha\alpha}]^{-1} \left(\{q_\alpha\} - [K_{\alpha\beta}]\{T_\beta\} \right) \tag{10}$$

3.3.4 Mechanical Model

The mechanical model is a FEM model made up of 3D Timoshenko beam elements. 3D beam elements are implemented to accurately represent the out of plane connection at the anchor from the device layer to the handle layer and back. Timoshenko beam theory was used due to the presence of shorter elements that are used to represent blocky portions of the device where transverse shear and rotary effects can be dominating and is not accounted for in Euler-Bernoulli beam theory [25]. Due to the symmetry of the device, only half of the actuator need to be analyzed with roller boundary conditions set at the center line. The visual representation of the model for the baseline design consisting of nodes and beam elements can be seen in Figure 3.6. A note is that node numbering overlapping occurs at the anchor portion as the result of having out of plane elements.

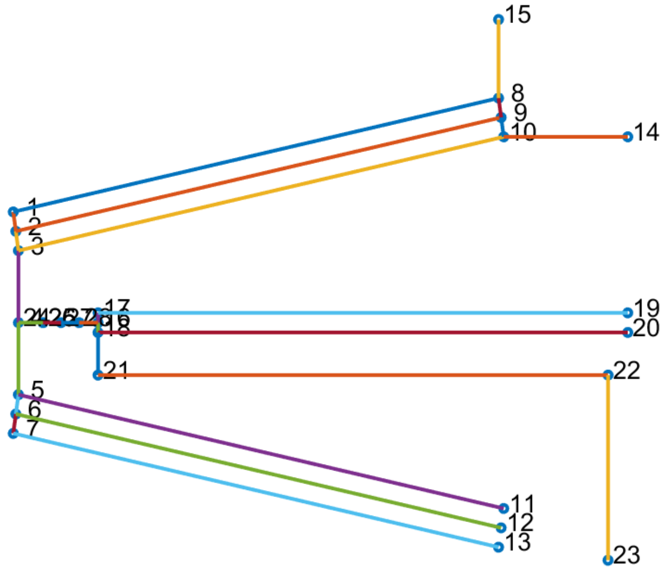

Figure 3.6: Visual representation of mechanical model for baseline design.

Similar to the thermal model, the governing matrix equation, Eq. 11, where $[K]$ is the global stiffness matrix assembled using all of the element stiffness matrices of the members, $\{D\}$ is the nodal displacement vector which can also be seen as boundary conditions and $\{R\}$ is the nodal forces vector which contains all external loads, needs to be solved to determine the beam structure's stiffness and nodal displacements.

$$[K]\{D\}=\{R\} \tag{11}$$

The element stiffness matrix for 3D Timoshenko beams is shown in Eq. 12 [24].

$$
[k]=\left[\begin{array}{cccccc|cccccc}
X & 0 & 0 & 0 & 0 & 0 & -X & 0 & 0 & 0 & 0 & 0 \\
 & Y_1 & 0 & 0 & 0 & Y_2 & 0 & -Y_1 & 0 & 0 & 0 & Y_2 \\
 & & Z_1 & 0 & -Z_2 & 0 & 0 & 0 & -Z_1 & 0 & -Z_2 & 0 \\
 & & & S & 0 & 0 & 0 & 0 & 0 & -S & 0 & 0 \\
 & & & & Z_3 & 0 & 0 & 0 & Z_2 & 0 & Z_4 & 0 \\
 & & & & & Y_3 & 0 & -Y_2 & 0 & 0 & 0 & Y_4 \\
\hline
 & & & & & & X & 0 & 0 & 0 & 0 & 0 \\
 & & & & & & & Y_1 & 0 & 0 & 0 & -Y_2 \\
 & & & & & & & & Z_1 & 0 & Z_2 & 0 \\
 & & \text{Symmetric} & & & & & & & S & 0 & 0 \\
 & & & & & & & & & & Z_3 & 0 \\
 & & & & & & & & & & & Y_3
\end{array}\right]
\begin{array}{c}
u_1 \\ v_1 \\ w_1 \\ \theta_{x1} \\ \theta_{y1} \\ \theta_{z1} \\ u_2 \\ v_2 \\ w_2 \\ \theta_{x2} \\ \theta_{y2} \\ \theta_{z2}
\end{array}
\qquad (12)
$$

The terms in the matrix are as follows: $X=\dfrac{AE}{L}$, $Y_1=\dfrac{12EI_Z}{(1+\phi_y)L^3}$, $Y_2=\dfrac{6EI_Z}{(1+\phi_y)L^2}$, $Y_3=\dfrac{(4+\phi_y)EI_Z}{(1+\phi_y)L}$, $Y_4=\dfrac{(2-\phi_y)EI_Z}{(1+\phi_y)L}$, $\phi_y=\dfrac{12EI_Z k_y}{AGL^2}$, $S=\dfrac{GK}{L}$ and the Z_i terms are defined the same way as the Y_i terms but with the subscripts of I and ϕ switched. E is the elastic modulus, I is the moment of inertia, A/k_y is the effective shear area for transverse shear deformation in the y direction, G is the shear modulus and K is a property of the shape and size of the cross section and is a fraction of the polar moment of inertia. As shown the matrix is 12 × 12 with 6 degrees of freedom at each end of the beams. Transformation matrices for orienting 3-D beam elements and converting their element stiffness matrices to global coordinates are constructed using direction cosines [26].

The stiffness of the actuator is defined in this instance as the vertical force applied at the tip of the actuator divided by the resultant displacement of the tip. This value can be calculated using the MATLAB program by applying an arbitrary load of 1 N at the tip and dividing the value by the tip displacement. To estimate the tip displacement from thermal expansion, temperature profiles generated using the thermal model is used as input. Based on the temperatures reached for each beam segment, external forces are applied at the end nodes such that the resulting axial strain matches the strain resulting from the thermal expansion. The equivalent loads applied at ends of beam elements is described by Eq. 13, where α is the thermal expansion coefficient. The thermal expansion coefficient is taken as a function of temperature based on Eq. 14 [27].

$$R = \alpha \cdot \Delta T \cdot E \cdot A \tag{13}$$

$$\alpha(T) = (3.725\{1 - \exp[-5.88 \times 10^{-3}(T - 124)]\} + 5.548 \times 10^{-4} T) \times 10^{-6} (\mathrm{K}^{-1}) \tag{14}$$

The model is solved in the same method as the stiffness calculation, with the exception that the thermal loads are converted to equivalent external mechanical loads, which produces the displacement result from thermal expansion. With the inherent stiffness as well as the tip displacement calculated, the two terms are multiplied to arrive at the actuation force which can also be interpreted as the force required to restrict the tip from displacing given that the device is being joule heated.

3.3.5 Failure Analysis

Additional functions of the model include stress and buckling analysis to ensure that no failure modes will occur based on a given voltage input. This is accomplished by applying the actuation force at the tip and finding the internal loads for each beam member. With the displacement at all nodes solved, the values can be plugged back into the individual element stiffness matrix equations to solve for element forces and moments. Normal, bending and shear stresses can be found with Eq. 15, where F is the normal force, M is the bending moment, y is the distance from the neutral axis, V is the shear force, Q is the statical moment of area and b is width of the material perpendicular to the shear.

$$\sigma_n = \frac{F}{A}$$
$$\sigma_b = \frac{My}{I} \tag{15}$$
$$\tau = \frac{VQ}{Ib}$$

In addition, normal forces on beam elements that are applied in compression are checked against the critical buckling load given by Eq. 16, where K is the column effective length factor based on the beam end boundary conditions.

$$P_{cr} = \frac{\pi^2 EI}{(KL)^2} \tag{16}$$

This capability assists in the estimation of appropriate operation parameters as well as resultant temperature ranges that do not meet or exceed potential failure criteria.

3.4 Optimization

The analytical model was incorporated into the Boundary Learning Optimization Tool (BLOT) [28] developed by our collaborators at UCLA which used the 11 independent parameters as the optimization inputs, the total actuation force and stroke as the optimization objectives, and the geometric constraints as the constraint functions. Stroke is calculated as the sum of the displacements of the tip in the expansion and in the compression mode. Actuation force is the product of the actuator stiffness and the tip displacement from thermal expansion in the two actuation modes, which can also be interpreted as the force required to restrict the tip from displacing given that the device is being joule heated. Figure 3.7 shows the cloud plot of the performances of different actuator geometries calculated using the analytical model, where each point corresponds to a distinct design.

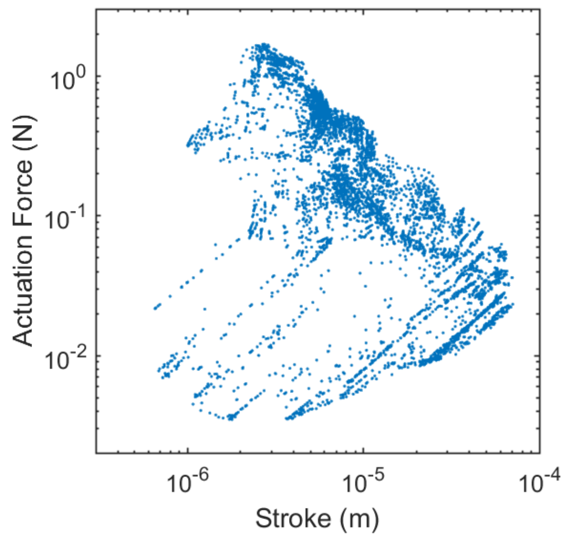

Figure 3.7: Cloud plot from optimization results for performance of actuator designs.

Four actuator geometries are selected from the optimization boundary for fabrication, ranging from one nearing highest force output to one nearing highest stroke while minimizing trade-off. They are marked in red in Figure 3.8 which shows the magnified portion of the minimum trade-off boundary slope.

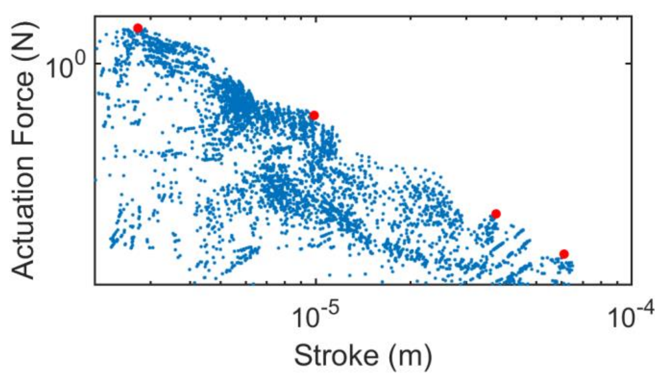

Figure 3.8: Magnified cloud plot with four selected designs marked in red.

The four selected designs can be seen in Figure 3.9. As shown, the designs can have drastically different appearances than the baseline design.

Device 1

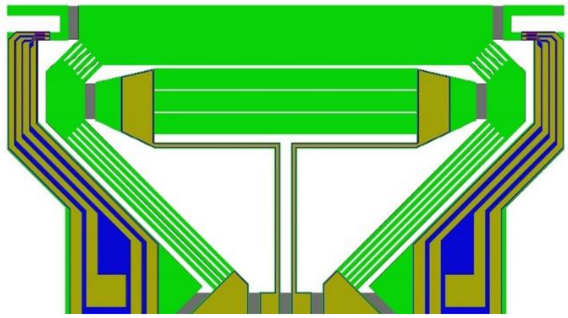

Device 2

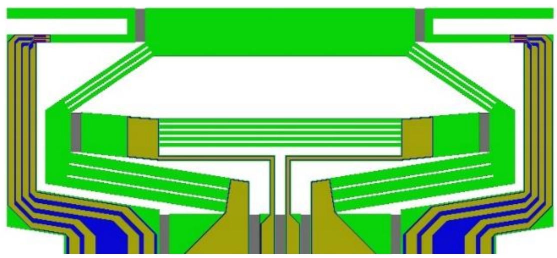

Device 3

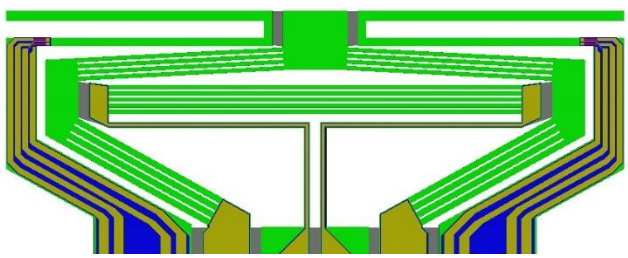

Device 4

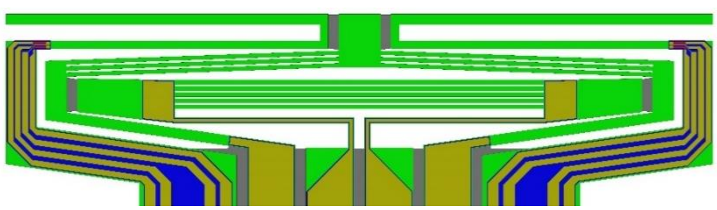

Figure 3.9: Four selected designs, ranging from highest stiffness/lowest travel (top, Device 1) to lowest stiffness/highest travel (bottom, Device 4).

3.5 FEA Verification

The four actuator geometries are further analyzed using COMSOL FEA software and results are compared with that from the analytical model. A sample electrothermal simulation for Device 4 in the expansion mode can be seen in Figure 3.10 with the temperature profile comparison shown in Table 3.1. Comparisons indicate that the thermal model is generally accurate with an overall overestimation of temperature. Results from the other selected three actuator designs are also favorable with percentage differences generally below 20% and can be found in Appendix C.

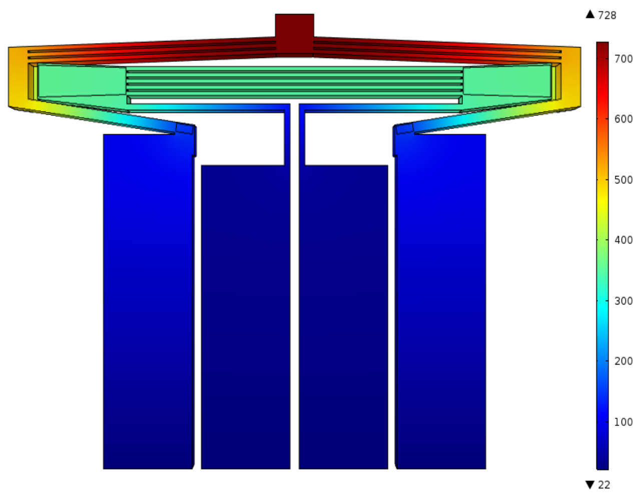

Figure 3.10: Temperature profile for Device 4 in expansion mode simulated in COMSOL.

Table 3.1: Temperature probes comparison for Device D in expansion.

Actuator #4 Temperatures	Expansion		
	FEA (ºC)	Model (ºC)	% Diff
TopBeamTipEnd	727.8	804.8	-10.6%
TopBeamAnchorEnd	505.2	536.9	-6.3%
TopBeamAvg	654.4	710.9	-8.6%
BottomBeamAnchorEnd	485.5	505.3	-4.1%
BottomBeamBaseEnd	139.8	131.9	5.7%
BottomBeamAvg	330.1	339.4	-2.8%
CenterBeamAvg	349.7	383.8	-9.7%
MiddleTopAvg	229.6	257.0	-11.9%
MiddleSideAvg	89.9	90.0	-0.1%
TipSideMin	727.9	805.6	-10.7%
TipBottomAvg	728.0	805.3	-10.6%

Similar to the analytical model, the device stiffness's were found in commercial FEA by applying an arbitrary load of 4 N (1 N at each corner) to the tip and dividing the value by the resultant tip displacement. A sample simulation for device 3 can be seen in Figure 3.11 and Table 3.2 shows the stiffness comparisons for the four selected actuator designs. The percentage difference is somewhat larger than that of the electrothermal model, however the same trend of decreasing stiffness's can be observed in both FEA and the analytical model. Furthermore, given the fact that the stiffness covers a very large range, from as low as around 3000 N/m to as high as around 1.8×10^6 N/m which is a factor of 600, the magnitude of the difference can be considered as relatively less dominant.

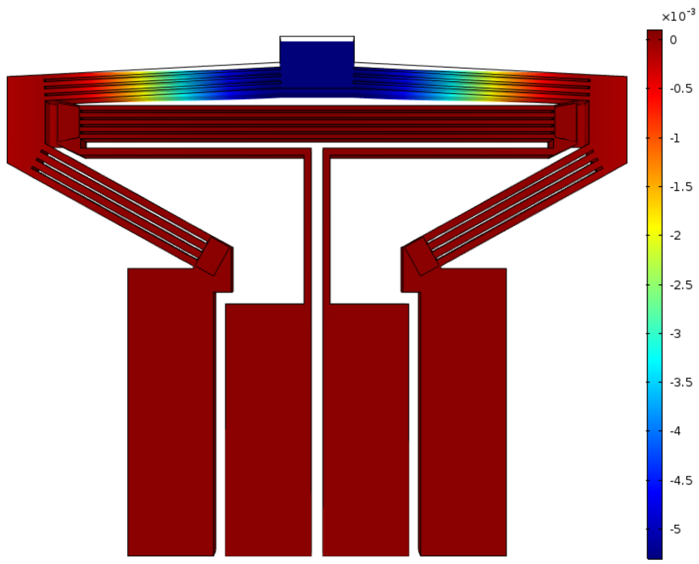

Figure 3.11: Simulation to calculate stiffness of device 3. Scale bar units is mm.

Table 3.2: Stiffness comparison for four selected designs.

Actuator #	FEA Stiffness (N/m)	Model Stiffness (N/m)	% Diff
1	1.81×10^6	2.25×10^6	-23.8%
2	1.41×10^5	1.79×10^5	-26.8%
3	7.57×10^3	8.55×10^3	-12.9%
4	2.89×10^3	2.40×10^3	16.9%

Finally, the results for the tip displacement from thermal expansion are compared. A sample simulation for the expansion of device 2 is shown in Figure 3.12 and Table 3 shows the tip displacement comparisons due to thermal expansion of the four selected actuator designs. With the exception of two cases in compression mode, the results are generally comparable with the expected trend of increasing tip displacement with decreasing stiffness present in both the analytical model and FEA.

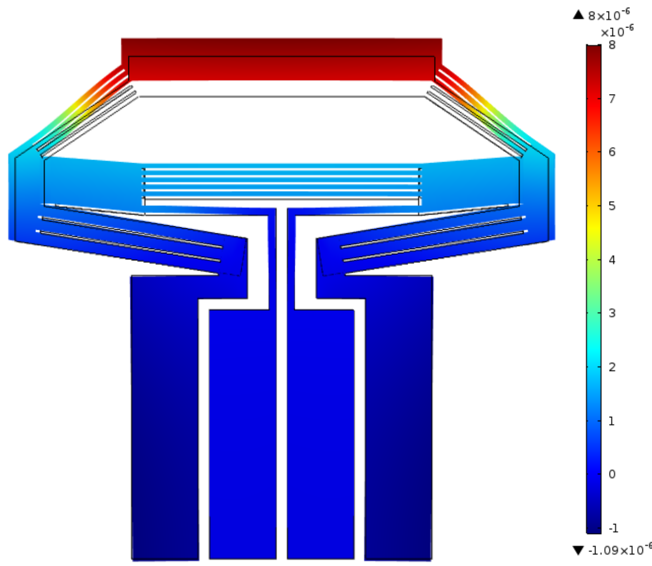

Figure 3.12: Simulation to determine tip displacement of device 2 under thermal expansion. Scale bar units is mm.

Table 3.3: Tip displacement comparison for four selected designs.

Actuator #	Expansion		
	FEA (µm)	Code (µm)	% Diff
1	3.03	2.65	12.6%
2	7.87	7.16	9.1%
3	18.97	18.15	4.3%
4	30.39	30.09	1.0%
	Compression		
	FEA (µm)	Code (µm)	% Diff
1	-1.04	-1.24	-19.4%
2	-7.27	-6.60	9.1%
3	-23.50	-31.11	-32.4%
4	-55.26	-48.90	11.5%

3.6 Discussion and Potential Improvements

As previously mentioned, the analytical model is a highly idealized examination of the actuators where the result accuracy is greatly affected by the limitations of bar and beam element FEM as well as various assumptions/approximations made. In the analytical model, approximations to certain geometrical dimensions and not necessarily beam-like features must be made as to represent the device as a bar/beam structure since they still contribute to the thermal and mechanical behavior. Furthermore, bar/beam FEM structures have idealized joints whereby elements are connected at a node, while meshes in higher order FEA are able to produce more accurate representation of connections. Degrees of freedom and boundary conditions also cannot be perfectly replicated in the analytical model due to the fact that they must be applied at nodes and are idealized beam end conditions. Moreover, certain beam theories are better suited depending on the scenario and the current version of the model only implements one type.

Specific to the thermal portion of the model, the theoretical calculation assumes that current passes through the entirety of the bar element cross-sectional areas while in commercial FEA and real life this assumption may not stand. Thus, it is likely that the general overestimation of the temperature in the analytical model is a result of this assumption of maximum joule heating, and with actuator designs that have beams with large cross-sectional areas, the difference of the results when compared to that of FEA would also be larger. The doping and in turn resistivity of the actuator beams are also considered to be homogenous throughout the device which is again an idealized assumption made in order to perform calculations. The realistic case of non-uniform doping would likely result in an unsymmetrical and irregular temperature profile which further conflicts with boundary conditions set in the mechanical model. Lastly, although not necessarily compatible with the analytical modelling method, convection and radiation as well as conduction with surrounding air should be taken into consideration.

Overall, since each step in the analytical model relies on previous calculations, notably the thermal model using the results from the electrical model as input and the mechanical model using the results from the thermal model as input, the errors from each step can cascade and magnify to greater proportions in the final result. Thus, it can be extremely difficult to achieve perfectly analogous results between the analytical model and FEA since the error must be kept at extremely small values at every step in the procedure. To improve the accuracy of both the analytical model and FEA, an iterative solution should be implemented where certain constants, such as resistivity and thermal conductivity, used in both modelling methods are instead incorporated as functions of temperature. Different combinations of boundary conditions can also be explored that may provide more realistic representations of how the devices function, such as looser restrictions regarding out of plane movement or allowing certain degrees of freedom at theoretically fixed supports. If time permits, optimization conducted purely through FEA software would likely produce more accurate results, however the analytical model appears to be consistent with general performance trends and is fairly accurate in its predictions, so it can suffice in terms of preliminary analysis and device selection.

Chapter 4: Fabrication

4.1 Overview

Fabrication of the devices was done in the Microelectronics Research Center at the J. J. Pickle Research Campus and standard microfabrication processes and commercial tools were used. Five photomasks were required and the order was fulfilled by Compugraphics. Mask design was done in AutoCAD where geometries of device layers were exported from SolidWorks, with the five layers being polysilicon, silicon nitride, gold, device side silicon and back side silicon. Five different device designs were selected for fabrication, including the four from optimization presented in the previous section and the baseline design. With two versions of each design for strain gauge configurations, there were a total of ten different devices to undergo fabrication. 100 mm diameter SOI wafers were used as the base substrate and each wafer houses 284 devices.

4.2 Process Flow

The process flow for the entire fabrication process can be seen in Figure 4.1. A description of each step is shown below. Recipes used in each step can be found in Appendix D with specific comments.

1. Start with SOI Wafer.
2. LPCVD 200 nm Silicon Nitride.
3. LPCVD 200 nm Polysilicon. HF dip. Diffusion dope $POCl_3$ (form PSG layer). Anneal to drive in dopant. Wet etch (BOE) PSG layer.
4. PR mask and plasma etch polysilicon.
5. PR mask and plasma etch silicon nitride.

6. Liftoff PR pattern. E-beam evaporation of gold, 200 nm. Liftoff.
7. Plasma etch back side polysilicon and silicon nitride.
8. ALD aluminum oxide 200 nm.
9. Back side hard mask pattern. Plasma etch back side aluminum oxide.
10. Front side hard mask pattern. Plasma etch front side aluminum oxide.
11. Deep silicon etch front side. Before large features reach 400 μm, dice wafer into 16 smaller pieces. Continue etching individual pieces.
12. Deep silicon etch back side. Plasma etch buried oxide layer from back side.
13. Plasma etch front side aluminum oxide to expose gold.

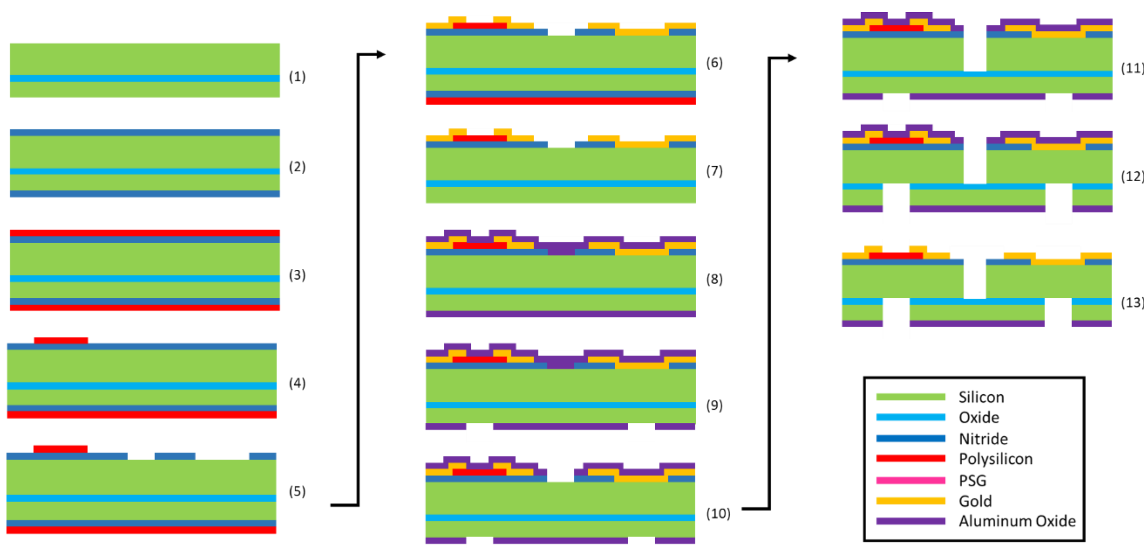

Figure 4.1: Process flow for fabrication process.

4.3 Deep Silicon Etch

Aside from minor and generally trivial obstacles, the fabrication process up to step 7 was completed in a relatively smooth manner. The most arduous step in the fabrication process is undoubtedly the device side deep silicon etch which required a considerable amount of recipe tuning and led to drastic alterations to the process flow that was originally planned. The tool used was the Plasma-Therm: VERSALINE DSE and it utilizes the Bosch process where passivation and etching steps are cycled through to achieve high aspect ratio deep silicon etch. A schematic showing the process of each cycle can be seen in Figure 4.2 [29]. First, in the deposition step, C_4H_8 gas is used to coat the exposed surfaces of the sample with the polymer passivation layer that protects the sidewalls from lateral etching in subsequent etch steps. The second step, a depassivation etching step, uses SF_6 as the etchant gas and is intended to selectively remove the passivation layer at the bottom of the trench by increasing the bias voltage and in turn the directional ion bombardment. The third and final step in the cycle is the isotropic etch of silicon at the bottom of the trench using the same etchant gas after the removal of the passivation layer.

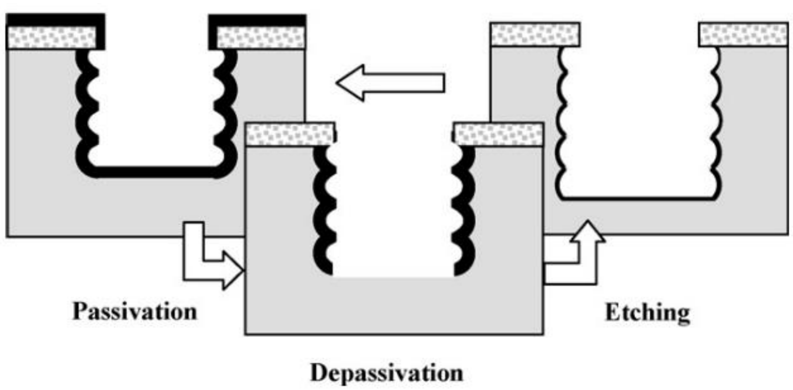

Figure 4.2: 3 Step cycle for deep silicon etching.

4.3.1 Aspect Ratio Dependent Etching and Sidewall Profile

A known phenomenon in deep reactive ion etching processes is the Aspect Ratio Dependent Etching (ARDE) effect, where bigger features will etch at a faster rate than that of smaller features. While fillers were added to areas of the device where large portions of silicon are to be etched, the feature sizes still varied from a minimum of 10 µm wide gaps between actuator beams to 50 μm wide trenches. Using the starting recipe, the profile of features can be seen in Figure 4.3.

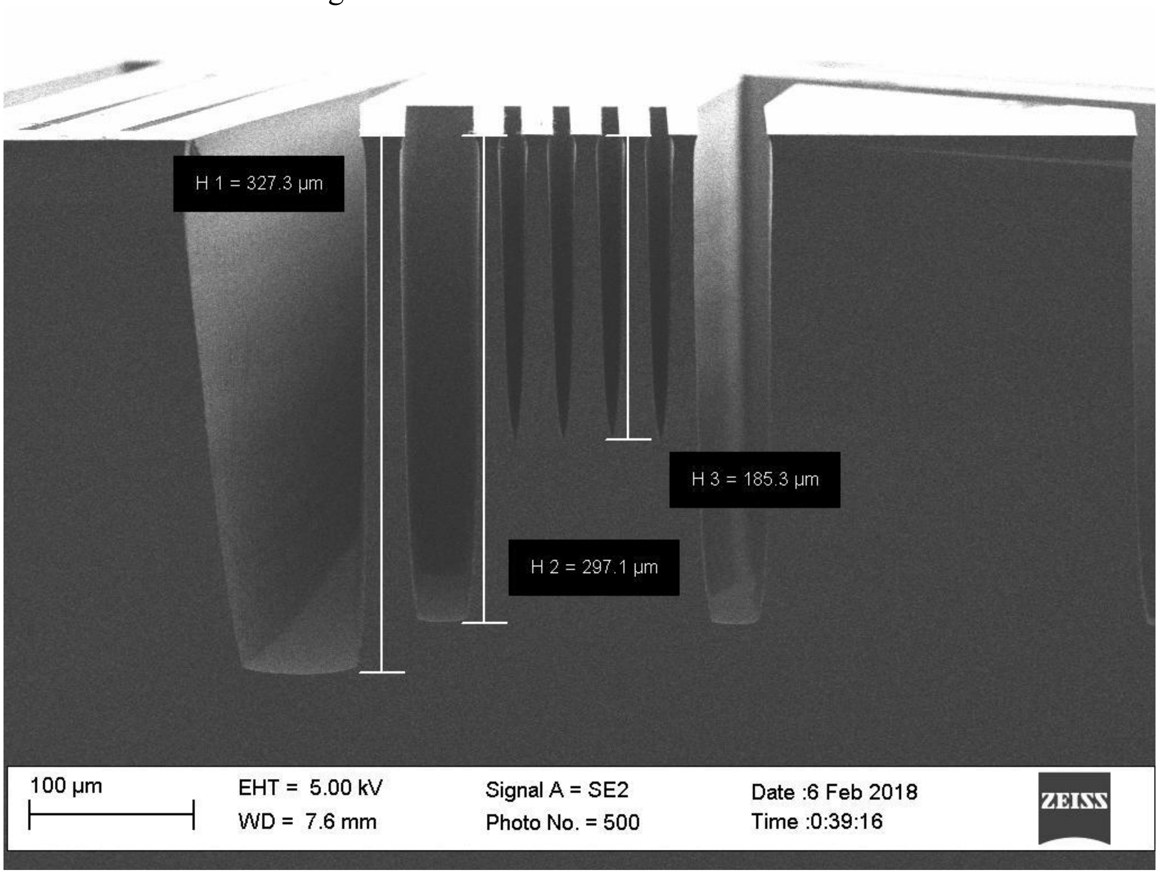

Figure 4.3: Etch profile using starting recipe.

As shown, the ARDE ratio between big and small features is about 1.6:1 with the sidewall having a positively tapered profile, especially for the small features. One reported method to mitigate the ARDE effect is to manipulate the timing ratio of the three stages in one cycle [30]. A schematic demonstrating the process can be seen in Figure 4.4, with the idea being that since the passivation polymer thickness during the deposition step is positively correlated with feature size, in that wider trenches will have thicker polymer deposition at the bottom, and the polymer removal step is independent of aspect ratio, an increase in the passivation and the first etching step relative to the second etching step essentially provides a head start for the etching of the smaller features to compensate the ARDE effect in the following isotropic etching step. In addition to adjusting the timing ratio, the RF bias during the depassivation step was also increased to facilitate the etching of the polymer.

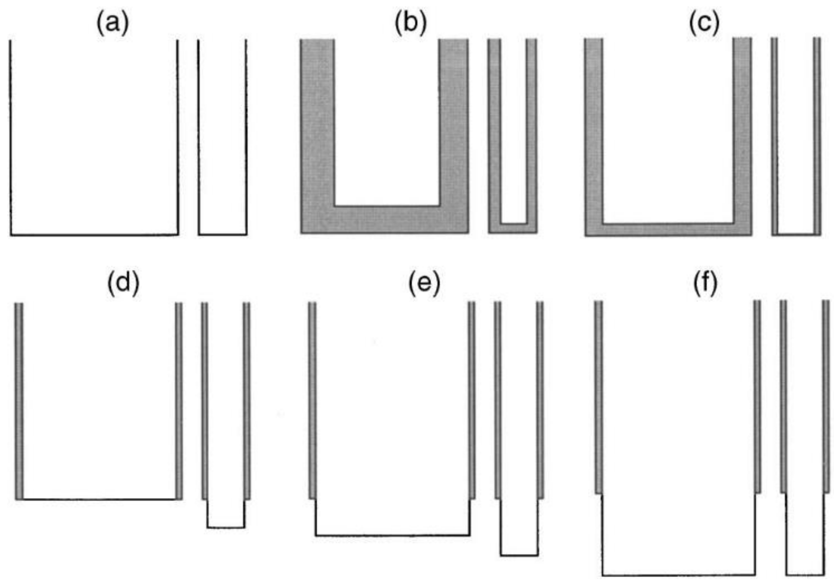

Figure 4.4: Schematic demonstrating method to mitigate ARDE [30].

In addition, to achieve vertical sidewalls, other modifications to the recipe were made including a higher ratio between etchant gas flow to passivation gas flow and a reduction to etchant gas pressure [31]. An SEM image showing the results of the modified recipe can be seen in Figure 4.5.

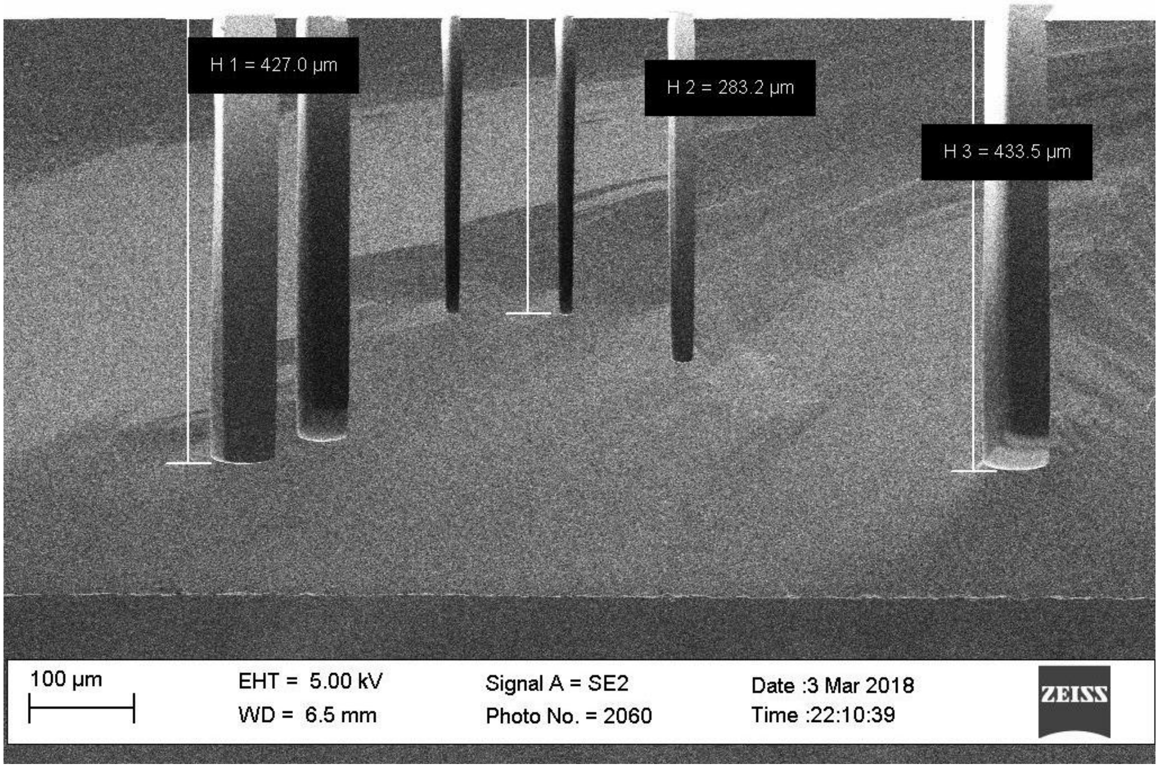

Figure 4.5: Etch profile using modified recipe.

As shown, the sidewall profile was improved drastically where the small features no longer converge sharply to a point due to positive tapering. The ARDE effect was reduced slightly to around 1.5:1 but can be considered as a decent improvement given that the etch depth was higher than that of Figure 4.3 and ARDE effect is expected to exacerbate with increasing etch depth. Theoretically, due to the presence of the buried oxide layer that effectively acts as an etch stop, the ARDE effect should not pose an issue for the etching of the actual device wafers. However, notching at the silicon/oxide interface [30] as well as thermal issues can occur so it is still desirable to reduce the ARDE effect as much as possible.

4.3.2 Masking Layer

Originally, after step 7, photoresist was chosen as the masking material for the deep silicon etch. It was initially theorized that a photoresist masking layer of around 10 µm thick would be sufficient to survive the 400 µm device side silicon etch and using photoresist would allow for a much easier process to strip the masking layer post-etch.

To test etch recipes, 100 mm diameter, 550 µm thick bare silicon wafers were used and a preset etch recipe was used as a starting point. As the etch is intended to be essentially through-wafer and to replicate the conditions of the device wafer etch, the test wafers were mounted to a handle wafer of equal size using photoresist and Fomblin oil as bonding material to prevent detached features from falling into the chamber and to prevent helium leaks into the chamber. 12 µm thick SPR 220 7.0 photoresist was used initially as the etch mask, however back-side helium pressurization and photoresist burning was a prominent issue. Images showing a sample progression can be seen in Figure 4.6.

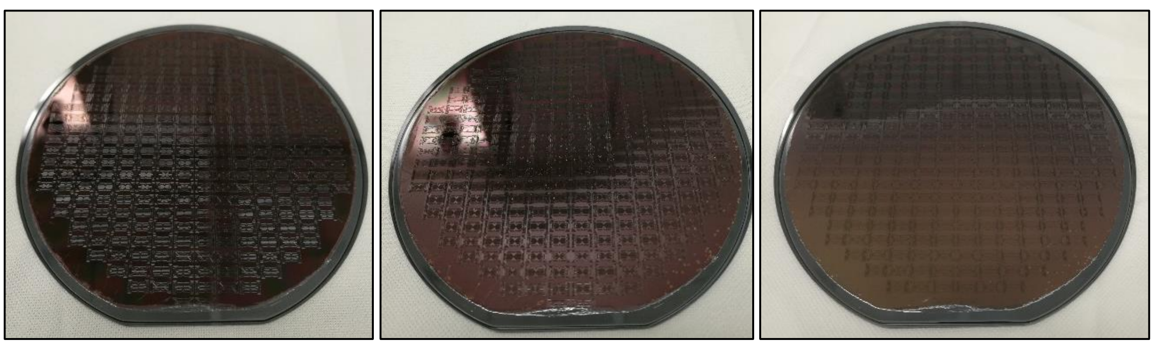

Figure 4.6: Sample progression of photoresist reticulation (burning). (Left) Original mask, (Center) after 325 cycles, (Right) after 925 cycles.

Thus, to alleviate burning of the resist, the recipe was tuned such that the ICP coil power was reduced from 3500 W to 1200 W to reduce the temperature of the chamber and wafer. With the change, the masking layer was able to reach higher number of cycles without as much reticulation. However, it was found that the photoresist on portions of the wafer would appear to be depleted at around 1200 cycles, shown in Figure 4.7.

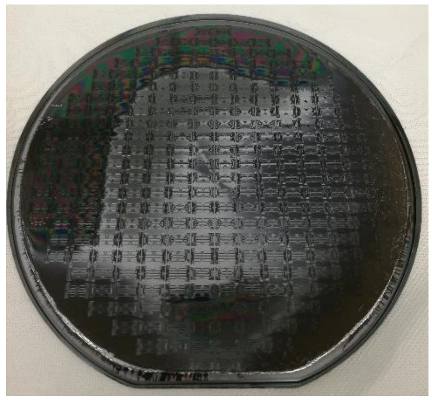

Figure 4.7: Sample etch with lower ICP power after 1200 cycles.

The etch was estimated to require around 1600 cycles for the small features to reach 400 μm so to ensure that the photoresist mask can survive through the etch cycles, a double coating recipe for SPR 220 7.0 was developed that resulted in a 20 μm thick masking layer. Surprisingly, even with the much thicker masking layer, the photoresist mask again underwent drastic reticulation and depletion at around 1200 cycles. An image showing the results can be seen in

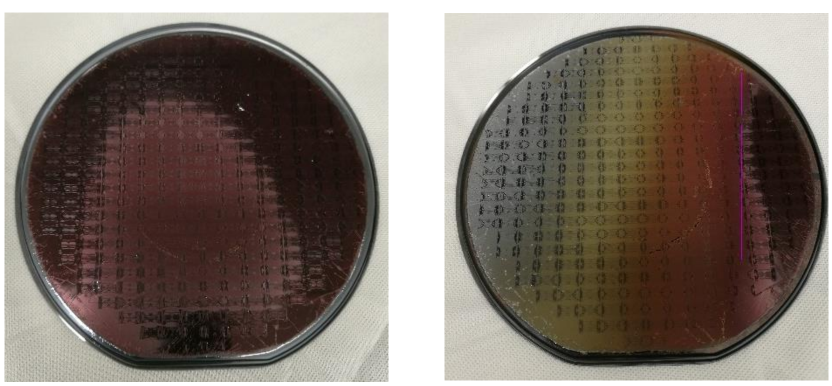

Figure 4.8: (Left) After 1200 cycles. (Right) After 1400 cycles.

After pondering upon the unexpected results, it was hypothesized that at around 1200 cycles, the rim around the perimeter of the wafer, which had to be cleared of photoresist to prevent the wafer from adhering to the clamping ring, had been etched through completely which led to a sudden poor thermal contact between the device wafer and the handle wafer. Thus, due to the increase in wafer temperature, the selectivity of the photoresist was reduced significantly [32] and the remaining amount was etched away in a small number of cycles.

Because it was believed that the issue cannot be resolved through the usage of a thicker photoresist masking layer as well as the fact that the burning of photoresist cannot be controlled or eliminated to a reasonable degree regardless of recipe parameters, a different masking material was sought. Aluminum oxide was selected as the hard mask material based on the necessity of high enough selectivity to survive 1600 cycles of the etch, limited suitable deposition methods due to the stage of progress in the fabrication process as well as the ability to be stripped away after the etch. Aluminum oxide was reported to have selectivity against Silicon up to 1:70000 in deep silicon etching (albeit at cryogenic temperatures) [33] and empirical testing indicated that 200 nm of the masking material can easily survive 1600 cycles. The deposition technique is also compatible with the state of the device wafers as the ALD is not a high temperature process nor does it involve any operations that can potentially damage the devices. Lastly, it can be etched away in an ICP etcher in a controlled manner.

It should be noted that measuring the exact etch selectivity of the masking material against silicon was difficult and relatively trivial due to the fact that the remaining thickness can only be measured by subtracting the feature height before and after stripping the material. Stripping the masking layer before the completion of the etch precludes any further etching which results in a massive time sink and waste of material. Furthermore, the profiler tip at the facility is not able to measure more than around 50 um deep for the smaller feature sizes so the actual etch depth can only be found at the approximated end of the etch when observed in the SEM, at which point the photoresist would not be able to be observed and the aluminum oxide would be much too thin in comparison to the etched silicon.

4.3.3 Further Thermal Issues

After finalizing the DSE recipe, switching etch mask material and testing with sample wafers, we proceeded with the processing for one of the device wafers. Originally, the device side etch was also planned to preceded by the back side etch due to the fact that the back side etch is only 50 μm deep and only has silicon that serve no other purpose than act as mechanical connections, meaning that handling of the back side can be much less stringent and will not require protection for the subsequent device side etch. The result of the etch was a complete failure where thinner actuator beams and smaller features were etched away completely as a result of severe undercut. Images of the failed process can be seen in Figure 4.9 and Figure 4.10.

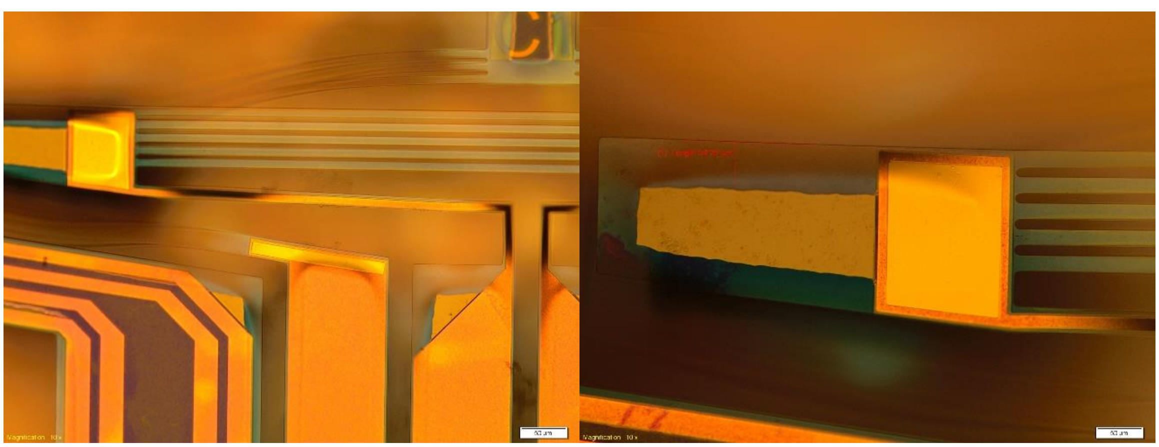

Figure 4.9: Microscope images of post-etch device with original process flow.

Figure 4.10: SEM images of post-etch device with original process flow.

As shown in Figure 4.9, the thin sheet of transparent green colored material is the remaining aluminum oxide mask and the actuator beams below have been etched away completely. The figure on the right indicates an undercut of around 55 μm at the anchor portion. The SEM images confirm that the beams have indeed been etched away and only the bottom portions have survived the severe undercut. It was hypothesized that the cause of this extreme discrepancy between device wafer and sample wafer results is again caused by thermal issues that greatly reduced the selectivity of the sidewall passivation. Because the back side etch was performed prior to the device side etch, there are 50 μm deep features at the bonding interface between the device wafer and the handle wafer. Since the photoresist used to bond the two wafers together cannot completely fill the cavities of the features, the thermal contact between the wafers is likely extremely poor and they could essentially act as hot trapped air pockets. Furthermore, due to ARDE, the buried oxide instead of silicon will be exposed to the plasma and etched for an extended period of time at the bigger features. The corresponding charging effects as well as charge separation due to the broken conductive current path [34] can further lead to increased wafer temperatures.

To combat these issues, the process was altered such that the device side deep silicon etch is conducted prior to the back side due to it being a more critical and tighter tolerance process. This change ensures good thermal contact between the device wafer and handle wafer due to not having features at the bonding interface. Furthermore, the wafer is diced into 16 smaller pieces with around 20 devices on each after around 800 cycles of the etch before any of the big features reach the buried oxide layer. Each piece is then etched individually for the remainder of the process which provides more opportunities to determine favorable processing parameters and avoids the elimination of entire wafers at a time due to failed attempts. Doing so also further promotes better thermal contact between the piece and handle wafer as mounting a whole 100 mm wafer onto a handle wafer of the same size is more prone to poor adhesion and incomplete contact. Lastly, shorter etching periods of 200 cycles instead of conducting the entire etch in one continuous sitting are implemented with added delay period of a few minutes between each set to allow for sufficient cooling of the chamber and wafer. With the implementation of these final changes to the process, successful fabrication of the devices was achieved and can be seen in Figure 4.11 and Figure 4.12.

Figure 4.11: (Left) Wafer piece with devices still attached. (Right) Device on SEM stub.

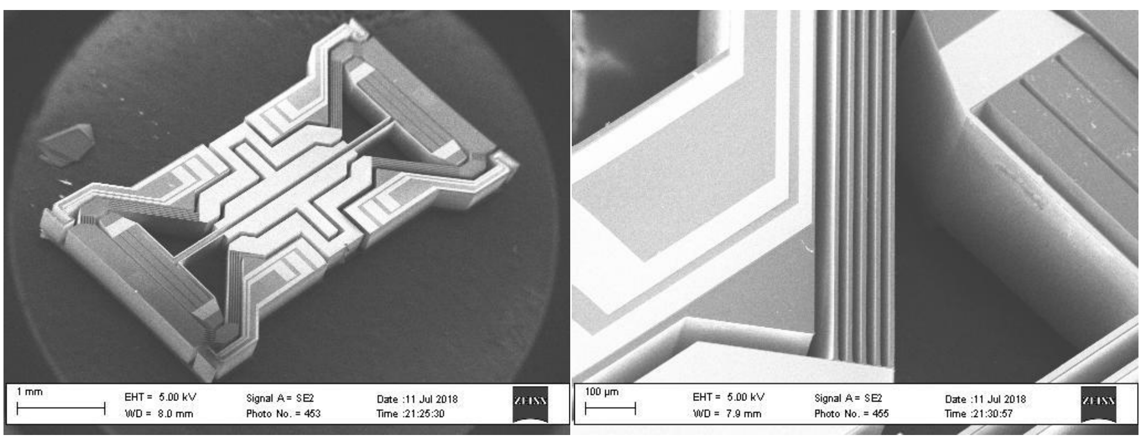

Figure 4.12: SEM image of sample device.

4.4 Discussion and Recommendations

While overall device fabrication was successful, features still suffer from minor undercut of around 2 µm. The quality of etch profiles are also unknown due to the need to cleave the completed devices if cross-sections are to be viewed. Repeatability of the process is also poor in that the degree of undercut can vary despite operating with the exact procedure and recipes. Currently, the process time required for the complete fabrication of one piece of the wafer is likely around three fully dedicated weeks, with the 400 μm deep silicon etching step leading in time consumption due to the short segmented etch periods with the added time of delays as well as reapplying mounting material. Lastly, it was found that results from sample etches using bare silicon wafers generally cannot be relied upon to predict that of SOI wafers. Certain issues only arise and become uncovered in the process of working on device wafers but due to the limited availability of SOI wafers and prior testing, they cannot be reliably foreseen.

Potential design changes that could facilitate the fabrication process include possibly having overall larger device footprints with minimum feature sizes of 25 μm instead of 10 μm. The small sizes of the devices give rise to difficulties in terms of handling as well as cleaving to observe cross section and recipe development for the deep silicon etch would also be much easier for larger features. It should also be emphasized that an effort should be made to make etch features to not simply be similar in dimensions but the exact same since ARDE is very sensitive and difficult to compensate for. Furthermore, due to the limitations of tools as well as other factors, looser tolerances on alignment and feature sizes would be desirable. Certain available mask aligners simply do not allow for very precise alignment in addition to the fact that coating/ liftoff and photolithography processes are often not perfect. Other wafer substrate options can also be explored with some potential sacrifices to performance, specifically instead of having a 400 μm thick silicon layer which necessitates a through-wafer level etch, a thinner device layer would be much easier to process.

Chapter 5: Preliminary Experimental Testing

5.1 Overview

At the time of this report, only 2 pieces out of the 16 have undergone complete fabrication and produced functional devices. Unfortunately, the pieces happened to only house two out of the five device designs, specifically design 1 and the baseline design. Therefore, device testing could only be performed on the two device designs and the remainder of the designs have not undergone performance validation.

5.2 Device Testing

Device testing was performed using the MPS150 manual probe system where direct contact was made between the probes connected to the sourcemeter and the gold electrodes. The devices were placed such that the center portion was secured onto a glass slide with the pressure applied by the probes and the actuator portion at one end is suspended off the edge to prevent any friction or restriction of movement. With two available probes, either the expansion or the compression can be activated at one time. The voltage supply had an upper limit of 20 V which is sufficient given the general theoretical operating voltage of around 15 V for the devices. Video footage of the microscope was recorded and used to determine the travel of the devices using a calibration length scale. Figure 5.1 shows the snapshots of the tip of device 1 before being powered and the point of maximum travel. Compression of around 2 μm for the baseline device was also observed but the displacement range is too small for data collection given the current metrology method.

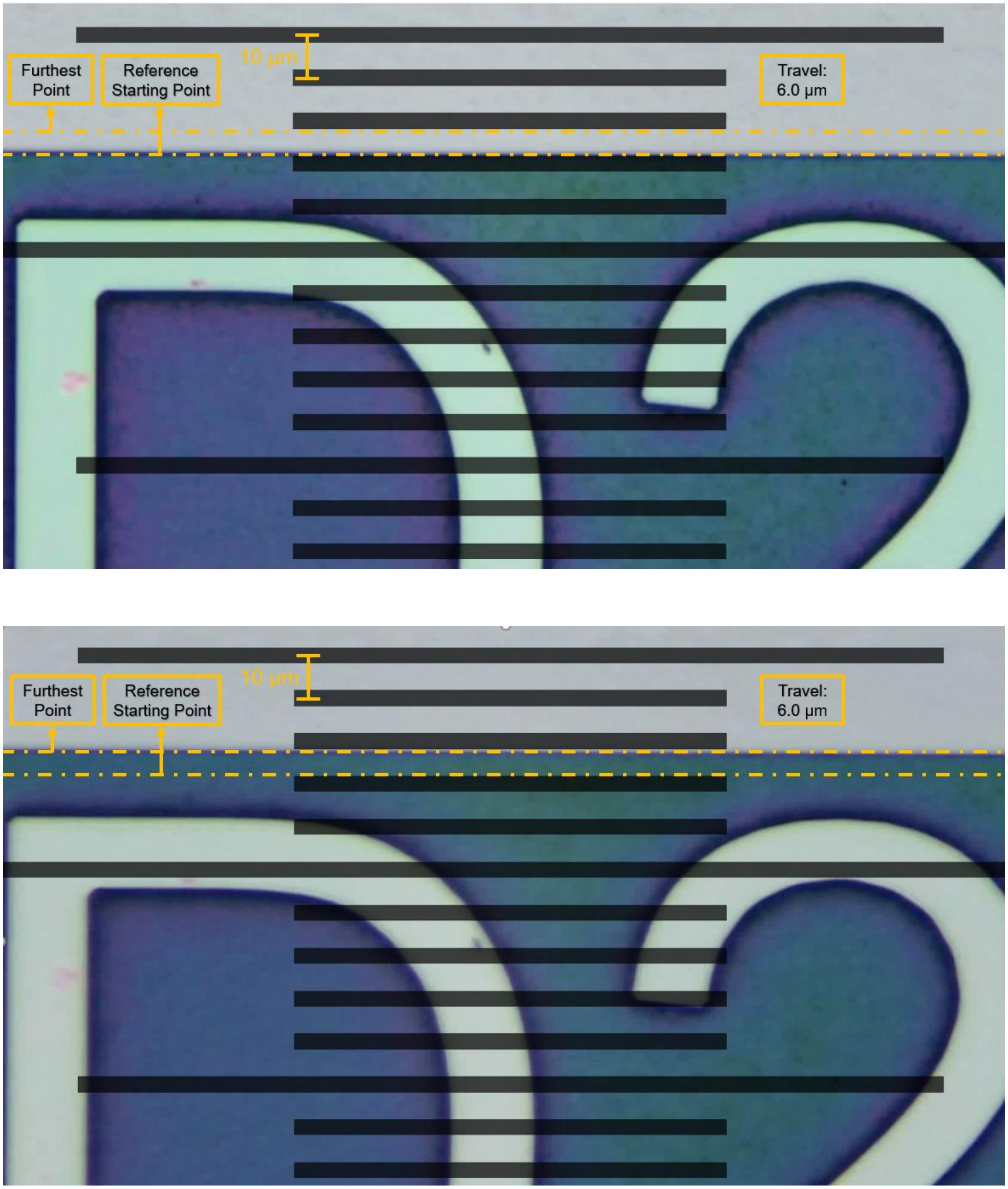

Figure 5.1: (Top) Unpowered tip position. (Bottom) Point of maximum travel.

Figure 5.2 shows the experimental tip displacement vs. voltage plots for the expansion of the device 1 and baseline device.

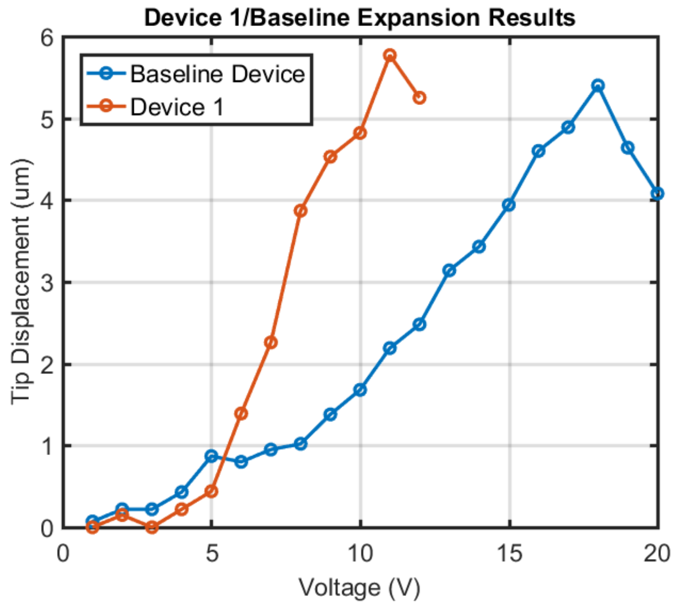

Figure 5.2: Experimental tip displacement vs. voltage results for device 1 and baseline device.

As shown in both instances, the tip displacement increases steadily in a generally linear manner with increasing voltage input up to a point of maximum travel, at which point the tip retracts even with increasing voltage. The positive travel of device 1 reached a maximum value of 5.8 µm which is larger than what was predicted by around 3 µm. The travel of the baseline device was predicted to be larger than that of device 1 which was demonstrated in an initial trial where the maximum travel reached 9.2 µm. However, voltage data was not collected for that test and the second trial using the same device, the data of which is shown in Figure 5.2, could not yield the same degree of displacement. Current values reached up to 0.3 A for device 1 and 0.1 A for the baseline device.

5.3 Discussion

Currently, repeated testing of devices is limited to possibly only two to three times with diminishing performance as mentioned previously with the baseline device as an example. It was observed that at higher voltage loads, the gold traces had begun to liquefy and bubble up which leads to the eventual burning/blackening of the material. This is the likely the cause of the non-repeatability of device testing and solutions to the problem may include the monitoring of device temperature to ensure that it does not pass a certain threshold or the deposition of a thicker gold layer which would reduce the resistance and in turn the temperature increase due to resistive heating.

A custom PCB board, shown in Figure 5.3, was designed for devices to be wire bonded to and interface with external circuity through a flat flex connector. Attempts at wire bonding has been unsuccessful, however, with the deposited gold on the device peeling off when contact with the bead is made. Potential causes include poor adhesion between the deposited gold and surfaces underneath or damage/contamination to the gold during fabrication processes. Other users of the probe station have reported better performance results, specifically higher actuation to voltage ratio, when devices are wire bonded instead of current supply made through direct probe contact which is another potential source of inaccuracy with the current testing method.

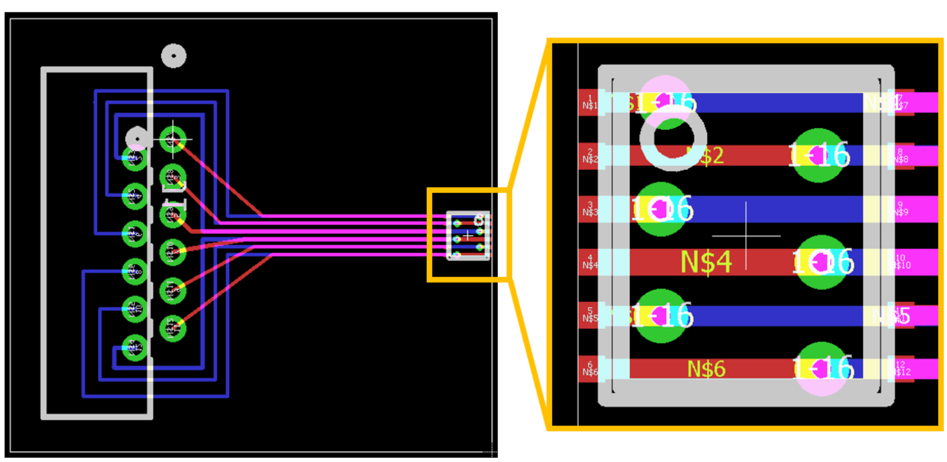

Figure 5.3: PCB design for half/full bridge configuration of device.

5.4 Future Work

Beyond the preliminary device testing procedure described above, many other device properties and performance factors need to be determined and validated. Thermal imaging to detect the temperature profiles of the devices during operation is possible with the probe station and should be compared to theoretical values. Inherent stiffness of the devices can also be found using nanomechanical characterization tools, such as the TriboIndenter TI 950 available at the Microelectronics Research Center. The piezoresistive strain gauges fabricated on the devices need to be confirmed as functional but require the preceded ability for the device to be wire bonded due to the limited number of probes available on the probe station. Following the successful detection of tip displacement using the strain gauges, feedback control scheme can be incorporated for the device in the TriboIndenter where the programmable stiffness capability of the device can be explored by inducing counterbalance force/displacements based on the loads generated by the tool.

Chapter 6: Conclusion

6.1 Project Summary

The goal of this project was to develop a MEMS thermal actuator to be incorporated as the constituent element of the unit cells for an microarchitectured material. A novel actuator design was contrived with bidirectional capabilities that adds range and versatility to shape morphing, complimented by high resolution sensing capabilities of piezoresistive strain gauges. An analytical model was created to facilitate design selection through optimization and four actuator geometries with minimum calculated trade-offs were selected for fabrication. Successful fabrication of the devices and preliminary testing results demonstrate the validity of the concept that would lead to a new level of miniaturization for the building blocks of microachitectured materials.

6.2 Future Work

In addition to the future testing described in Section 5.4, the most critical upcoming work would be the fabrication and testing of the remainder of the devices so that the performance trade-offs of the four selected designs can be observed and compared. Metrology methods with higher accuracy as well as repeatability studies on actuator performance need to be conducted to firmly validate its applicability as a viable unit cell building block. Examination on the functionality of the piezoresistive strain gauges is also required to set the groundwork for the implementation of active control.

Assembly of a unit cell prototype is another sought after goal since it is required to arrive at the final product of a microarchitectured material. Small cubes that would represent the IC's would be machined and devices would be adhered to each of its six faces. Completed unit cells can then be congregated to form the actual material and provide insight into what the final product would look like. Going beyond the visual prototype, the development of the IC's that would power and control each of the actuators is of course another great milestone to the true realization of this technology.

Other future work includes investigations into fabrication consistency. Currently the fabrication process still has varying degrees of uncertainty where seemingly same processes produces different results. A more systematic study of the processes would be greatly beneficial to improve manufacturing efficiency and rate of success as well as lay the foundation for potential mass production.

As mentioned previously, performance evaluation using commercial FEA software is likely more accurate than the analytical model due to many of its limitations. Thus, the current selected actuator designs derived from optimization using the analytical model may not actually be the best performing and a selection of optimized devices using commercial FEA can be fabricated for potential improvement.

Lastly, the investigation into the actuators have generally been in the static and steady state domains. Further understanding of the transient thermal responses, switching speed, dynamic properties and other aspects associated with real time operation would be immensely valuable.

Appendices

APPENDIX A: SOI WAFER SPECIFICATIONS

Device Layer:	
Diameter:	100 +/- .2mm
Type/Dopant:	P/Boron
Orientation:	<1-0-0>+/-.5 degree
Thickness:	50 +/- 0.5 um
Resistivity:	0.005 - 0.020 ohm-cm
Edge Exclusion:	<5mm
Particles:	<10@0.2um
Flats:	Semi Std.
Finish:	Polished
Buried Thermal Oxide:	
Thickness:	**4um +/- 5%**
Handle Wafer:	
Diameter:	100 +/- .2mm
Type/Dopant:	P/Boron
Orientation:	<1-0-0>+/-.5 degree
Thickness:	400 +/- 10 um
Resistivity:	0.005 - 0.020 ohm-cm
Flatness:	<2um
Flats:	Semi Std.
Finish:	Polished

APPENDIX B: RANGE AND RESOLUTION FOR OPTIMIZATION VARIABLES

	Lower Limit	Upper Limit	Resolution
Number of Center Beams (#)	1	25	1
Length of Center Beams (µm)	0.1	2.5	0.01
Width of Center Beams (µm)	0.02	0.1	0.01
Angle of Lower Beams (^{o})	1	45	1
Number of Lower Beams (#)	1	25	1
Length of Lower Beams (µm)	0.1	2.5	0.01
Width of Lower Beams (µm)	0.02	0.1	0.01
Angle of Upper Beams (^{o})	1	45	1
Number of Upper Beams (#)	1	25	1
Length of Upper Beams (µm)	0.1	2.5	0.01
Width of Upper Beams (µm)	0.02	0.1	0.01

APPENDIX C: ANALYTICAL MODEL TEMPERATURE PROFILES

Actuator #1	Expansion			Compression		
	FEA (ºC)	Model (ºC)	% Diff	FEA (ºC)	Model (ºC)	% Diff
TopBeamTipEnd	656.12	714.45	-8.9%	436.12	583.78	-33.9%
TopBeamAnchorEnd	636.62	691.97	-8.7%	455.09	583.78	-28.3%
TopBeamAvg	648.83	703.39	-8.4%	442.22	583.78	-32.0%
BottomBeamAnchorEnd	617.10	665.79	-7.9%	411.14	564.98	-37.4%
BottomBeamBaseEnd	286.72	279.43	2.5%	141.64	195.30	-37.9%
BottomBeamAvg	480.97	499.73	-3.9%	279.56	380.14	-36.0%
CenterBeamAvg	507.41	515.26	-1.5%	826.53	1130.03	-36.7%
MiddleTopAvg	398.43	420.03	-5.4%	625.34	883.39	-41.3%
MiddleSideAvg	182.29	185.32	-1.7%	279.73	375.45	-34.2%
TipSideMin	656.21	822.12	-25.3%	440.24	583.78	-32.6%
TipBottomAvg	677.28	786.23	-16.1%	441.85	583.78	-32.1%
Actuator #2	Expansion			Compression		
	FEA (ºC)	Model (ºC)	% Diff	FEA (ºC)	Model (ºC)	% Diff
TopBeamTipEnd	1071.0	1033.9	3.5%	329.4	416.1	-26.3%
TopBeamAnchorEnd	812.9	707.9	12.9%	356.4	416.1	-16.8%
TopBeamAvg	971.1	886.8	8.7%	337.9	416.1	-23.2%
BottomBeamAnchorEnd	727.0	635.9	12.5%	326.0	391.4	-20.0%
BottomBeamBaseEnd	454.7	378.3	16.8%	181.2	223.6	-23.4%
BottomBeamAvg	600.7	513.6	14.5%	247.5	307.5	-24.3%
CenterBeamAvg	553.0	516.5	6.6%	787.0	826.3	-5.0%
MiddleTopAvg	402.6	390.6	3.0%	514.9	545.3	-5.9%
MiddleSideAvg	183.6	169.3	7.8%	230.5	231.1	-0.3%
TipSideMin	1071.8	1173.9	-9.5%	337.7	416.1	-23.2%
TipBottomAvg	1090.7	1127.2	-3.4%	337.7	416.1	-23.2%
Actuator #3	Expansion			Compression		
	FEA (ºC)	Model (ºC)	% Diff	FEA (ºC)	Model (ºC)	% Diff
TopBeamTipEnd	801.0	926.2	-15.6%	273.3	303.2	-11.0%
TopBeamAnchorEnd	575.2	635.4	-10.5%	290.5	303.2	-4.4%
TopBeamAvg	723.2	820.2	-13.4%	278.9	303.2	-8.7%
BottomBeamAnchorEnd	515.4	589.4	-14.4%	270.1	289.1	-7.0%
BottomBeamBaseEnd	248.0	263.8	-6.4%	115.2	123.7	-7.4%
BottomBeamAvg	391.4	437.8	-11.9%	186.6	206.4	-10.6%
CenterBeamAvg	414.5	404.2	2.5%	797.1	1043.3	-30.9%
MiddleTopAvg	294.5	295.6	-0.4%	496.1	655.9	-32.2%
MiddleSideAvg	120.2	114.7	4.6%	191.5	236.7	-23.6%
TipSideMin	801.3	929.3	-16.0%	278.8	303.2	-8.7%
TipBottomAvg	801.7	928.2	-15.8%	278.8	303.2	-8.7%
Actuator #4	Expansion			Compression		
	FEA (ºC)	Model (ºC)	% Diff	FEA (ºC)	Model (ºC)	% Diff
TopBeamTipEnd	727.8	804.8	-10.6%	369.4	416.4	-12.7%
TopBeamAnchorEnd	505.2	536.9	-6.3%	393.9	416.4	-5.7%
TopBeamAvg	654.4	710.9	-8.6%	377.4	416.4	-10.4%
BottomBeamAnchorEnd	485.5	505.3	-4.1%	387.3	400.5	-3.4%
BottomBeamBaseEnd	139.8	131.9	5.7%	87.8	90.4	-3.0%
BottomBeamAvg	330.1	339.4	-2.8%	225.8	245.4	-8.7%
CenterBeamAvg	349.7	383.8	-9.7%	768.8	783.8	-1.9%
MiddleTopAvg	229.6	257.0	-11.9%	437.6	447.3	-2.2%
MiddleSideAvg	89.9	90.0	-0.1%	157.8	145.1	8.0%
TipSideMin	727.9	805.6	-10.7%	377.3	416.4	-10.4%
TipBottomAvg	728.0	805.3	-10.6%	377.3	416.4	-10.4%

APPENDIX D: FABRICATION PROCESS RECIPES AND COMMENTS

1. Start with SOI wafer.

2. Nitride Layer.
   a. Piranha clean
   b. MRL LPCVD Silicon Nitride Furnace
      Recipe: LS_Nit. Deposition time: 1.5 hr. 200 nm thickness.

3. Polysilicon Layer.
   a. Piranha clean
   b. MRL LPCVD Amorphous Silicon Furnace
      Recipe: AMP150. Deposition time: 1 hr 15 min. 200 nm thickess.
   c. Piranha clean
   d. HF (1:20) dip – 15 s.
   e. Diffusion Doping $POCl_3$ – MRL.
      Recipe: $POCl_3$ 9_7. Process time: 20 min.
   f. Anneal (Doped) – MRL
      Recipe: 1050_Ann. Process time: 30 min.
   g. Buffered Oxide Etch – 30 s.
   h. Use 4 point probe to measure sheet resistance. Measured value is around 0.75×10^2 Ω/□.

4. Etching polysilicon layer.
   a. Piranha clean if necessary. Otherwise Acetone + Methanol + Isopropanol Alcohol (AMI) clean.
   b. 2 µm thick AZ 1518 Photoresist Recipe – Polysilicon Pattern
      i. YES HMDS Oven.
      ii. Programmable Spinner. 500 RPM, 1000 Ramp, 5 s. 3500 RPM, 1000 Ramp, 30 s.
      iii. Hotplate. 115 ºC, 4 min.
      iv. Delay 10 min.
      v. Karl Suss MA6 Mask Aligner. 365 nm, 7.5 mW, hard contact, 15 µm alignment gap, 21 s exposure.
      vi. Hotplate. 115 ºC, 30 s.
      vii. MF 26A Developer. 30 s.
      viii. Hotplate. 115 ºC, 2 min.
   c. Etcher RIE 790 PlasmaTherm
      Recipe: Silow2. Process time: 4 min.
      Notes: If not etched through, add time until nitride layer is visible. Use kapton tape to secure wafer within chamber.

5. Etching silicon nitride layer.
   a. Piranha clean if necessary. Otherwise AMI clean.
   b. 2 µm thick AZ 1518 Photoresist Recipe – Silicon Nitride Pattern
   c. Etcher RIE 790 PlasmaTherm
      Recipe: Ta_Nit. Process time: 7 min. Rotate wafer 180 ºC. Another etching process for 7 min.
      Notes: If not etched through, add 5 min until silicon layer is visible. Use kapton tape to secure wafer within chamber.

6. Gold Layer.
   a. Piranha clean if necessary. Otherwise AMI clean.
   b. Liftoff photoresist recipe – Gold Pattern
      i. YES HMDS Oven.
      ii. LOR 5A Photoresist. Programmable Spinner. 500 RPM, 1000 Ramp, 5 s. 3500 RPM, 1000 Ramp, 30 s.
      iii. Hotplate. 115 ºC, 6 min.
      iv. Delay 5 min.
      v. 2 µm AZ 1518 Photoresist Recipe without HMDS, up to exposure step.
      vi. Karl Suss MA6 Mask Aligner. 365 nm, 7.5 mW, hard contact, 20 µm alignment gap, 22 s exposure.
      vii. Hotplate. 115 ºC, 30 s.
      viii. MF 26A Developer. 25 s. Add increments of 1 s if not developed completely.
   c. CHA E-Beam Evaporator
      Recipe: Gold w/ Tungsten Crucible. Process time: Varies. Depending on recipe settings deposition rate can reach 1.5 A/s. Deposit as much as possible, at least 200 nm thick.
      Notes: May need to require increase of maximum power or else deposition rate can be zero.
   d. Liftoff
      i. Prepare multiple Remover PG baths. Heat to upwards of 80 ºC. Soak wafers with agitation. Change to new Remover PG bath after half an hour. Soak up to another hour with agitation and proceed based on how much material has been lifted off.
      ii. If necessary, use sonicator with wafer in acetone bath, preferably with wafer in a wafer carrier facing down so that detached particles do not adhere to top surface.
      iii. Notes: Another reported method is to sonicate without solution for 5 seconds prior to first Remover PG soak to create cracks for the solution to seep through more effectively. The remaining procedure is the same. Avoid using sonicator unless absolutely necessary as lifted off gold particles can adhere to the surface and cannot be cleaned off later.

7. Etching backside polysilicon and silicon nitride layer.
    a. AMI clean.
    b. 2 µm thick AZ 1518 Photoresist Recipe on device side up to exposure step.
    c. Etcher RIE 790 PlasmaTherm
       Recipe: same as for device side.

8. Aluminum oxide hard mask.
    a. AMI clean followed by PVA TePla 300 Microwave Plasma asher to clear organic material from both sides of wafer.
    b. Cambridge NanoTech SavannahTM 200 ALD
       Recipe: Al2O3. Deposition rate is 1.1 A/cycle. Deposit around 200 nm.
       Note: need to use glass slide to prop up the wafer in the chamber so that the backside gets deposited with Al_2O_3 as well. Quality of backside mask is not critical.

9. Etching back side aluminum oxide
    a. AMI clean followed by Asher Nordson March PX-250 to clear organic material from back side of wafer.
    b. 10 µm AZ 9260 Photoresist Recipe – Back side Pattern
        i. YES HMDS Oven.
        ii. Programmable Spinner. 500 RPM, 1000 Ramp, 5 s. 2000 RPM, 1000 Ramp, 45 s.
        iii. Hotplate. 115 ºC, 4 min.
        iv. Rehydration. Submerge wafer in DI wafer for 15 mins.
        v. Karl Suss MA6 Mask Aligner. Backside alignment. 365 nm, 7.5 mW, hard contact, 25 µm alignment gap, 125 s exposure.
        vi. AZ 400K Developer diluted 1:4. 5-6.5 min development. Increase time if necessary.
        vii. Hard bake. 20 min 90 ºC hotplate.

       Note: Take out bottle containing photoresist from fridge, open lid to equalize pressure and reseal, and rest in room temperature for half an hour prior to spin. Prepare developer solution beforehand. Pour photoresist instead of using pipet. Hard bake temperature higher than 90 ºC tend to cause rounding of features. EVG 620 Mask Aligner can be used alternatively to MA6 for potentially better backside alignment.
    c. ICP Oxford 100 Etcher
       Recipe: Al2O3 BCl3 Ar Etch. Etch rate 3-7 nm/min, unstable. Etch until silicon layer below is visible.

10. Etching device side aluminum oxide
    a. AMI clean followed by Asher Nordson March PX-250 to clear organic material from device side of wafer.
    b. 10 µm AZ 9260 Photoresist Recipe – Front side Pattern

c. ICP Oxford 100 Etcher
   Recipe: Al2O3 BCl3 Ar Etch. Etch until silicon layer below is visible.

11. Device side deep silicon etch
   a. AMI clean followed by Nordson March PX-250 asher to clear organic material from device side of wafer.
   b. Attach wafer to handle wafer. Handle wafer should have aluminum oxide or silicon oxide deposited to prevent etching into them.
      i. Piranha/AMI clean handle wafer
      ii. Use quartz wafer with kapton tape at three points on edge of wafer to ensure device wafer and quartz wafer do not make contact. Tape quartz wafer to device wafer with device wafer back side exposed.
      iii. Spin AZ 5209E onto back side of device wafer with quartz wafer interfacing with the chuck. Can use manual spinner, 500 RPM for 5 s and 800 RPM for 30 s. Immediately detach device wafer from quartz wafer and place onto handle wafer.
      iv. Secure two wafers by pressing down with tweezers along perimeter and using clean wipe and something with large surface area to gently press them together.
      v. Bake at around 100 ºC for 1 min.
   c. Plasma-Therm: VERSALINE DSE
      Recipe:

Page: Setpoints

Parameter	1:CZ_Mounted D	2:CZ_Mounted D	3:CZ_Mounted D	4:CZ_Mounted D	5:CZ_Mounted D	6:CZ_Mounted D
Process Time Setpoint	30	5	2	3	0.8	5
OverEtchTimePercent	0.0	0.0	0.0	0.0	0.0	0.0
Pressure/Position/Evac Control	#pressure	#pressure	#pressure	#pressure	#pressure	#position
Pressure	10.0	10.0	30.0	35.0	45.0	0.0
Throttle Valve Position Setpoint	0.0	0.0	0.0	0.0	0.0	100
Process End Condition	#Time	#Time	#Time	#Time	#Time	#Time
Recipe Restart Sequence Name						
C4F8	50	50	100	100	100	0
SF6	50	50	75	100	150	0
Ar	30	30	30	30	30	0
O2	0.0	0.0	0.0	0.0	0.0	0.0
CF4	0.0	0.0	0.0	0.0	0.0	0.0
Gas 1 Dump Valve Direction	#To PM'	#To PM'	#To PM'	#To Pump'	#To Pump'	#To PM'
Gas 2 Dump Valve Direction	#To PM'	#To Pump'	#To Pump'	#To PM'	#To PM'	#To PM'
Helium Cooler Mode	#Pressure	#Pressure	#Pressure	#Pressure	#Pressure	#Flow
Helium Cooler Pressure Setpoint	4000.0	4000.0	4000.0	4000.0	4000.0	0.0
Helium Cooler Flow Setpoint	0.0	0.0	0.0	0.0	0.0	0.0
Bias RF Voltage Setpoint	0.0	50	10	240	10	0
Bias RF Waveform Setpoint	1	1	1	1	1	1

Page: Setpoints All

Parameter	1:CZ_Mounted D	2:CZ_Mounted D	3:CZ_Mounted D	4:CZ_Mounted D	5:CZ_Mounted D	6:CZ_Mounted D
Helium Cooler Mode	#Pressure	#Pressure	#Pressure	#Pressure	#Pressure	#Flow
Helium Cooler Pressure Setpoint	4000.0	4000.0	4000.0	4000.0	4000.0	0.0
Helium Cooler Flow Setpoint	0.0	0.0	0.0	0.0	0.0	0.0
Bias RF Voltage Setpoint	0.0	50	10	240	10	0
Bias RF Waveform Setpoint	1	1	1	1	1	1
ICP RF Forward Power Setpoint	0.0	1200	1200	1200	1200	0
ICP Match Control Mode	#Manual	#Automatic	#Hold	#Hold	#Hold	#Hold
ICP Match Load Position Setpoint	30	0.0	0.0	0.0	0.0	0.0
ICP Match Tune Position Setpoint	74	0.0	0.0	0.0	0.0	0.0
Temperature Electrode Setpoint	10	10	10	10	10	10
Temperature Lid Setpoint	140	140	140	140	140	140
Temperature Liner Setpoint	70	70	70	70	70	70
Temperature Spool Setpoint	175	175	175	175	175	175
Execute if later step restarted	true	true	false	false	false	false
External Detector Endpoint Recipe	#None	#None	#None	#None	#None	#None
Throttle Valve Overshoot Hold Time	0	0	0	0	0	0
Throttle Valve Overshoot	0.0	0.0	0.0	0.0	0.0	0.0

Cycles consist of loops through steps 3-5. Run 200 cycles of recipe in each segment with 5 min of delay time in between. Etch a total of 800 cycles.
Notes: After each O2 clean, chamber is hot and should be allowed to cool prior to first etching segment. Backside helium pressure and flow must be at reasonable values or else it is indication of thermal issues. With two wafers being clamped the backside helium pressure set point may need to be adjusted.

d. Soak device wafer in acetone or Remover PG if stubborn until separated from handle wafer.
e. Spin on protective PR layer using AZ 5209E recipe on device side and dice wafer into 16 smaller pieces using dicing saw.
f. AMI clean followed by Nordson March PX-250 asher for piece to be etched.
g. Clean handle wafer followed by a dehydration bake.
h. AZ 5209E recipe on handle wafer.
i. Attach device wafer piece onto center area of handle wafer. Clean all PR around the piece.
j. Plasma-Therm: VERSALINE DSE
Same recipe as before. 50 cycles each segment with 3-5 min of delay in between each. Etch until total cycles reach 1600, including cycles etched as whole wafer.
k. Soak in acetone/Remover PG until piece is separated from handle wafer.

12. Back side deep silicon etch and buried silicon oxide etch
a. AMI clean followed by Asher Nordson March PX-250 to clear organic material from back side of wafer.
b. Attach piece to handle wafer in the same fashion as for the front side.
c. Plasma-Therm: VERSALINE DSE

Same recipe as before. 50 cycles each segment with 3-5 min of delay in between each. Etch until total cycles reach 200.

d. Oxford 80 RIE Etcher
Recipe: SiO_2. Etch rate 28 nm/min.
Notes: Keep piece on handle wafer. Can go directly from the DSE to this etch.
e. Soak in acetone/Remover PG until piece is separated from handle wafer.

13. Front side aluminum oxide etch
a. AMI clean of piece followed by Asher Nordson March PX-250 asher if necessary.
b. ICP Oxford 100 Etcher
Recipe: Al_2O_3 BCl_3 Ar Etch. Etch until gold layer is exposed.

References

[1] L. A. Shaw and J. B. Hopkins, “An Actively Controlled Shape-Morphing Compliant Microarchitectured Material,” *J. Mech. Robot.*, vol. 8, no. 2, p. 021019, 2015.

[2] Q. Wang, J. A. Jackson, Q. Ge, J. B. Hopkins, C. M. Spadaccini, and N. X. Fang, “Lightweight Mechanical Metamaterials with Tunable Negative Thermal Expansion,” *Phys. Rev. Lett.*, vol. 117, no. 17, 2016.

[3] B. Haghpanah, H. Ebrahimi, D. Mousanezhad, J. Hopkins, and A. Vaziri, “Programmable Elastic Metamaterials,” *Adv. Eng. Mater.*, vol. 18, no. 4, pp. 643–649, 2016.

[4] H. Kurokawa, S. Murata, E. Yoshida, K. Tomita and S. Kokaji, "A 3-D self-reconfigurable structure and experiments," *Proceedings. 1998 IEEE/RSJ International Conference on Intelligent Robots and Systems. Innovations in Theory, Practice and Applications (Cat. No.98CH36190)*, Victoria, BC, Canada, 1998, pp. 860-865 vol.2.

[5] J. Bishop *et al*., "Programmable parts: a demonstration of the grammatical approach to self-organization," *2005 IEEE/RSJ International Conference on Intelligent Robots and Systems*, Edmonton, Alta., 2005, pp. 3684-3691.

[6] P. White, V. Zykov, J. Bongard, and H. Lipson, “Three Dimensional Stochastic Reconfiguration of Modular Robots,” *Robotics: Science and Systems I*, Aug. 2005.

[7] Y. Song, P. C. Dohm, B. Haghpanah, A. Vaziri, and J. B. Hopkins, “An Active Microarchitectured Material that Utilizes Piezo Actuators to Achieve Programmable Properties,” *Adv. Eng. Mater.*, vol. 18, no. 7, pp. 1113–1117, 2016.

[8] D. J. Bell, T. J. Lu, N. A. Fleck, and S. M. Spearing, “MEMS actuators and sensors: observations on their performance and selection for purpose,” *Journal of Micromechanics and Microengineering*, vol. 15, no. 7, 2005.

[9] G. T. A. Kovacs, *Micromachined Transducers Sourcebook*. New York: McGraw-Hill, 2000.

[10] J. J. Allen, *Micro electro mechanical system design*. Boca Raton, FL: Taylor & Francis, 2005.

[11] L. Que, J.-S. Park, and Y. B. Gianchandani, “Bent-beam electro-thermal actuators for high force applications,” *Tech. Dig. IEEE Int. MEMS 99 Conf. Twelfth IEEE Int. Conf. Micro Electro Mech. Syst. (Cat. No.99CH36291)*, no. 608, pp. 31–36, 1999.

[12] L. Que, J. S. Park, and Y. B. Gianchandani, "Bent-beam electrothermal actuators-Part I: Single beam and cascaded devices," *J. Microelectromechanical Syst.*, vol. 10, no. 2, pp. 247–254, 2001.

[13] H. Föll, "MEMS Sensors and Actuators," in *Hyperscript to: Semiconductor Technology*.

[14] C. Livermore, "Design choices: MEMS actuators," in *MIT OpenCourseWare*.

[15] T. Chu Duc, J. F. Creemer, and P. M. Sarro, "Lateral nano-Newton force-sensing piezoresistive cantilever for microparticle handling," *J. Micromechanics Microengineering*, vol. 16, no. 6, 2006.

[16] R. M. Panas, M. A. Cullinan, and M. L. Culpepper, "Design of piezoresistive-based MEMS sensor systems for precision microsystems," *Precis. Eng.*, vol. 36, no. 1, pp. 44–54, 2012.

[17] P. French and A. Evans, "Piezoresistance in polysilicon and its applications to strain gauges," *Solid-State Electronics*, vol. 32, no. 1, pp. 1–10, 1989.

[18] P. J. French, "Polysilicon: A versatile material for microsystems," *Sensors Actuators, A Phys.*, vol. 99, no. 1–2, pp. 3–12, 2002.

[19] R. Cragun and L. Howell, "Linear thermomechanical microactuators," *Asme Imece Mems*. pp. 181–8, 1999.

[20] Y. Zhu, A. Corigliano, and H. D. Espinosa, "A thermal actuator for nanoscale in situ microscopy testing: Design and characterization," *J. Micromechanics Microengineering*, vol. 16, no. 2, pp. 242–253, 2006.

[21] A. K. Gupta, "Circuit Solver using MATLAB Programming," *MATLAB By Examples*, 04-Nov-2011.

[22] X. J. Hu, A. Jain, and K. E. Goodson, "Investigation of the natural convection boundary condition in microfabricated structures," *Int. J. Therm. Sci.*, vol. 47, no. 7, pp. 820–824, 2008.

[23] R. Hickey, M. Kujath, and T. Hubbard, "Heat transfer analysis and optimization of two-beam microelectromechanical thermal actuators," *J. Vac. Sci. Technol. A Vacuum, Surfaces, Film.*, vol. 20, no. 3, pp. 971–974, 2002.

[24] R. . Cook, D. . Malkus, M. . Plesha, and R. . Witt, *Concepts and Applications of Finite Element Analysis*. 2002.

[25] Q. Wang and K. M. Liew, "Application of nonlocal continuum mechanics to static

analysis of micro- and nano-structures," *Phys. Lett. Sect. A Gen. At. Solid State Phys.*, vol. 363, no. 3, pp. 236–242, 2007.

[26] W. McGuire, R. H. Gallagher, and H. Saunders, "Matrix Structural Analysis," *J. Mech. Des.*, vol. 104, no. 3, p. 529, 1982.

[27] Y. Okada and Y. Tokumaru, "Precise determination of lattice parameter and thermal expansion coefficient of silicon between 300 and 1500 K," *Journal of Applied Physics*, vol. 56, no. 2, pp. 314–320, 1984.

[28] A. Hatamizadeh, Y. Song, and J. B. Hopkins, "Optimizing the Geometry of Flexure System Topologies Using the Boundary Learning Optimization Tool," *Math. Probl. Eng.*, vol. 2018, 2018.

[29] R. Abdolvand and F. Ayazi, "An advanced reactive ion etching process for very high aspect-ratio sub-micron wide trenches in silicon," *Sensors Actuators, A Phys.*, vol. 144, no. 1, pp. 109–116, 2008.

[30] S. L. Lai, D. Johnson, and R. Westerman, "Aspect ratio dependent etching lag reduction in deep silicon etch processes," *Journal of Vacuum Science & Technology A: Vacuum, Surfaces, and Films*, vol. 24, no. 4, pp. 1283–1288, 2006.

[31] M. Kumar, M. Wadhwa, S. Verma, M. M. Nayak, P. J. George, and A. K. Paul, "A systematic study of DRIE process for high aspect ratio microstructuring," *Vaccum*, vol. 84, no. 9, pp. 1142–1148, 2010.

[32] Ayón A. A., "Characterization of a Time Multiplexed Inductively Coupled Plasma Etcher," *Journal of The Electrochemical Society*, vol. 146, no. 1, p. 339, 1999.

[33] K. Grigoras, L. Sainiemi, J. Tiilikainen, A. Säynätjoki, V.-M. Airaksinen, and S. Franssila, "Application of ultra-thin aluminum oxide etch mask made by atomic layer deposition technique," *Journal of Physics: Conference Series*, vol. 61, pp. 369–373, Jan. 2007.

[34] S. Lai, S. Srinivasan, R. J. Westerman, D. Johnson, and J. J. Nolan, "Notch reduction in silicon on insulator (SOI) structures using a time division multiplex etch processes," *Micromachining and Microfabrication Process Technology X*, 2005.